VI. ICRF HEATING

D. B. BATCHELOR (ORNL), M. D. CARTER (ORNL), R. H. GOULDING (ORNL), D. J. HOFFMAN (ORNL), J. C. HOSEA (PPPL), E. F. JAEGER (ORNL), S. M. KAYE (PPPL), T. K. MAU (UCLA), C. K. PHILLIPS (PPPL), P. M. RYAN (ORNL), J. E. SCHARER (University of Wisconsin), D. W. SWAIN (ORNL), J. S. TOLLIVER (ORNL), J. R. WILSON (PPPL), and J. J. YUGO (ORNL)

VI.A. INTRODUCTION

Radio-frequency (RF) power in the ion cyclotron range of frequencies (ICRF) has been chosen as the primary auxiliary heating technique for BPX. This decision is based on the wide success of ICRF heating in existing large-scale experiments (JET, TFTR, JT-60), the capability of ion cyclotron waves to penetrate the high-density plasmas of BPX, the ability to concentrate ICRF power deposition near the plasma center, and the ready availability of high-power sources in the appropriate frequency range. The primary task of the ICRF system is to heat to fusion temperatures. However, other important roles are envisaged, such as the stabilization of sawteeth, preheating of the plasma during current rampup, and study of plasma current profile control by means of fast-wave current drive. It is essential that the ICRF system be capable of coupling power to the plasma effectively for all planned operating modes and that the ICRF system not rely on the tokamak to provide an ideal plasma tailored for ICRF heating.

The baseline heating scenario is to use ^{3}He minority in the D-T fuel plasma. At full field, $B_0 = 9$ T, this requires $f_{RF} \sim 90$ MHz. In lower field operation, $B_0 = 6$ T, ^{3}He minority at $f_{RF} \sim 60$ MHz and hydrogen minority at $f_{RF} \sim 90$ MHz will be used. The RF system will provide at least 20 MW coupled to the plasma in the frequency range of 60 to 90 MHz for pulses at least 15 s long. This is to be provided by 16 power sources. The possibility of an upgrade to 30 MW will be accommodated in the facility design. Operation in the range $f_{RF} = 120$ to 135 MHz may also be possible at reduced power, permitting hydrogen minority or second-harmonic deuterium heating at full field.

Section VI.B describes ICRF physics as applied to heating of BPX: heating scenarios, experimental results from present tokamaks, power absorption, partitioning of power between various plasma species, and tail formation. The detailed RF system design is presented in the System Design Description. However, the antenna is the critical interface between the RF system and the fusion plasma. The amount of power that can be coupled to the plasma per antenna determines the number of antennas (and ports) as well as the design of the feed system and number of power sources. For fixed voltage handling capability, this power level is proportional to the antenna loading resistance, which is itself critically dependent on the plasma density profile near the antenna. Therefore, Sec. VI.B describes the physics of antenna design issues, particularly estimates of antenna loading.

VI.B. ICRF PHYSICS

VI.B.1. ICRF Heating Scenarios

The standard operating scenario for bulk heating at full toroidal field ($B_0 = 9$ T) is to use ^{3}He minority heating in a bulk plasma consisting of 50-50 D-T. To place the minority resonance on axis requires an RF frequency between 85 and 92 MHz, depending on the Shafranov shift and plasma paramagnetism. Figure 6.1 shows the variation of cyclotron resonance frequency for various species across the

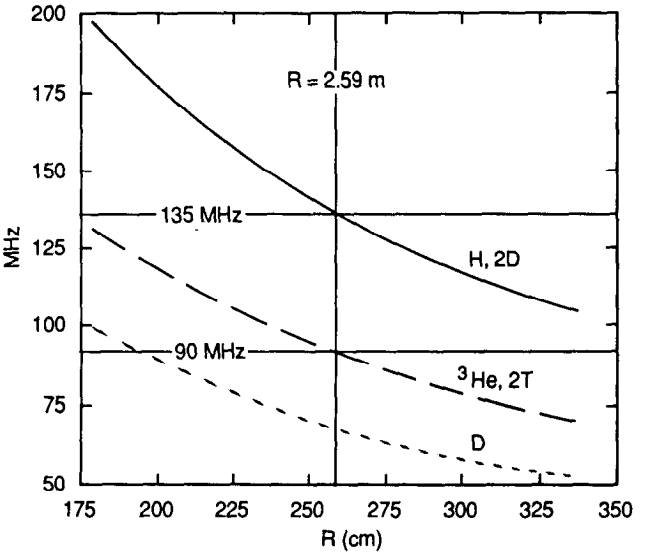

Fig. 6.1. Cyclotron frequency of various plasma species versus major radius, $B_0 = 9$ T.

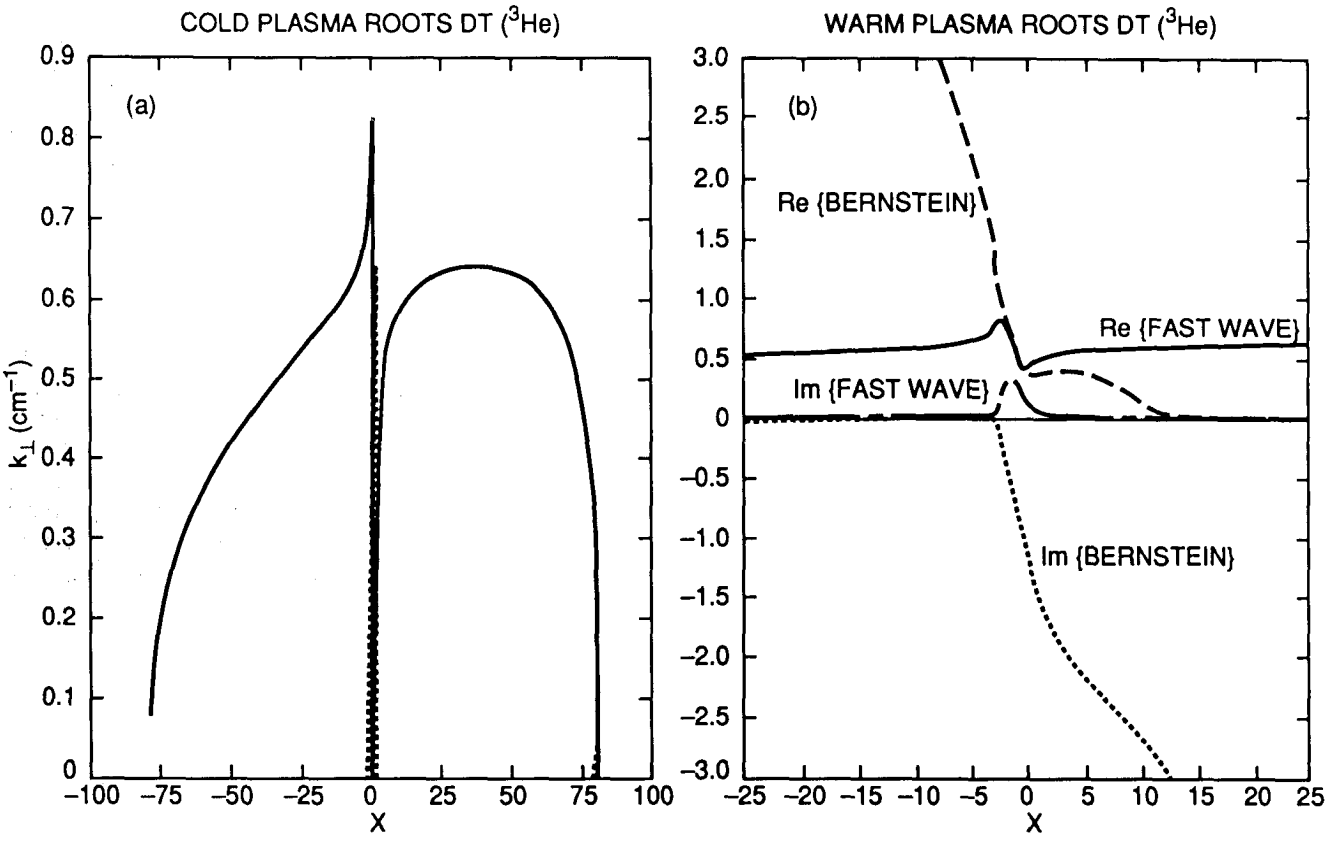

Fig. 6.2. Solutions of the dispersion relation $k_\perp$ for ^{3}He minority in D-T versus distance from the magnetic axis, $n_e(0) = 2 \times 10^{20}$ m^{-3}, $B_0 = 9$ T, $k_\parallel = 10$ m^{-1}, $\eta_{^3He} = 0.025$: (a) cold plasma and (b) warm plasma, $T_e = T_i = 10$ keV.

plasma cross section for $B_0 = 9$ T assuming vacuum magnetic fields ($B \propto 1/R$).

Figure 6.2a shows a plot of the fast-wave perpendicular wave number $k_\perp$ obtained from the cold plasma dispersion relation versus distance x from the machine center ($R = 2.59$ m) in the equatorial plane. The parameters were $n_e(0) = 2 \times 10^{20}$ m^{-3}, $B(0) = 9$ T, $k_\parallel = 10$ m^{-1}, $\eta_{^3\mathrm{He}} = 0.025$, $\eta_D = \eta_T = 0.475$, and $f_{\mathrm{RF}} = 90$ MHz. With these parameters, the ^{3}He cyclotron resonance is at $x = 5$ cm, and the ion-ion hybrid resonance is at $x = 0$. A thin evanescent layer ($k_\perp$ imaginary, dotted curve) lies between the ion-ion hybrid layer and the fast-wave cutoff. There are no other cold plasma resonances, but there are evanescent zones in the low-density edge regions. Figure 6.2b shows solutions of the warm plasma dispersion relation near the resonance for the parameters above, with $T_e = T_i = 15$ keV. One can see the coupling to the short-wavelength Bernstein made (chain dotted curve) on the high-field ($x < 0$) side of the hybrid resonance. At this temperature, the fast-wave cutoff and hybrid resonance pair have been resolved by resonance broadening and mode conversion. Both fast-wave reflection and transmission are quite small.

With ^{3}He resonant on axis, there are no hydrogen resonances in the device, although there is a deuterium resonance inboard of the machine center ($R = 1.8$ to 2 m). As the bulk plasma beta rises, direct second-harmonic heating of the tritium component, which coincides with the ^{3}He resonance, takes over. At the high densities employed on BPX, and because of the enhanced collisionality of ^{3}He^{++}, strong tail formation is not expected. This will result in bulk heating of the background ions rather than electrons.

With the high plasma current of BPX, confinement of tail populations is not expected to be an issue in any case, but will certainly not be important for ^{3}He. Because the wave power propagates essentially radially inward from the antenna and since density gradients provide an additional refractive focusing, the wave energy and subsequent absorption is concentrated near the plasma center. The presence of the shear Alfvén resonance near the inboard edge is an issue for further study, although this heating mode is routinely used in present tokamaks and no deleterious effects have been seen. The concern is that, due to the incomplete one-pass absorption for the ^{3}He minority mode, edge absorption might occur at the shear Alfvén resonance, which could give an undesirable heating profile or cause impurity problems.

At 2/3 field ($B_0 = 6$ T), two heating modes are available, minority ^{3}He at $f_{\mathrm{RF}} = 56$ to 61 MHz and minority hydrogen at $f_{\mathrm{RF}} = 85$ to 91 MHz. Figure 6.3 shows the variation of cyclotron resonance frequency for various species across the plasma cross section for $B_0 = 6$ T. Again, with ^{3}He resonant on axis, there are no hydrogen resonances in the device although the deuterium resonance appears on the inside region ($R = 1.8$ to 2 m). With hydrogen minority, a tritium second-harmonic resonance appears on the inside edge of the plasma for Shafranov shifts greater than a few centimeters. However, the one-pass absorption for the hydrogen minority mode is so large (~100%) that no significant edge heating should occur.

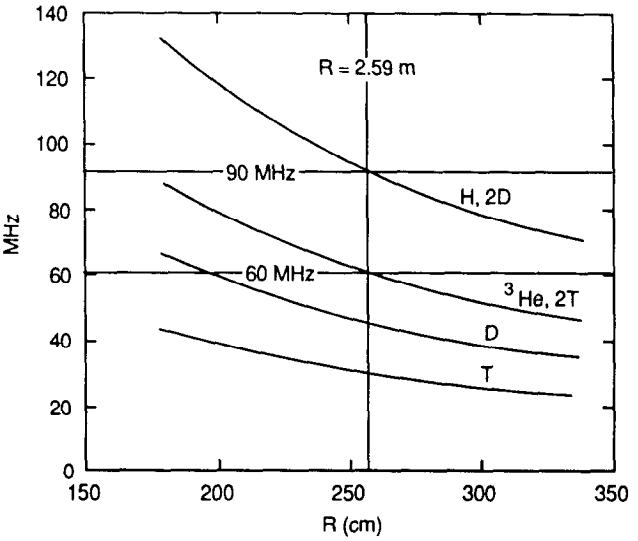

Fig. 6.3. Cyclotron frequency of various plasma species versus major radius, $B_0 = 6$ T.

VI.B.2. Summary of Recent Experimental Results

By now there is a considerable data base on ICRF with both ^{3}He minority and hydrogen minority modes at quite high power levels and plasma parameters. Some of the most encouraging results have come from JET, where up to 22 MW has been coupled to the plasma.[1] Temperatures of $T_e(0) = 11.5$ keV and $T_i(0) = 8$ keV have been achieved with 18 MW in limiter discharges, where peaked density profiles created by pellet fueling are maintained for long periods of time (>1 s). Very significant for BPX is that long, edge-localized mode (ELM) free H modes have been achieved with ICRF alone on JET (Ref. 2). Figure 6.4 shows an RF-produced H mode of 1.3-s duration in a double-null X-point discharge with $I_p = 3$ MA, $B_T = 2.8$ T, and $P_{\mathrm{RF}} = 7$ MW. The electron temperature reaches 9.5 keV at the end of the H mode,

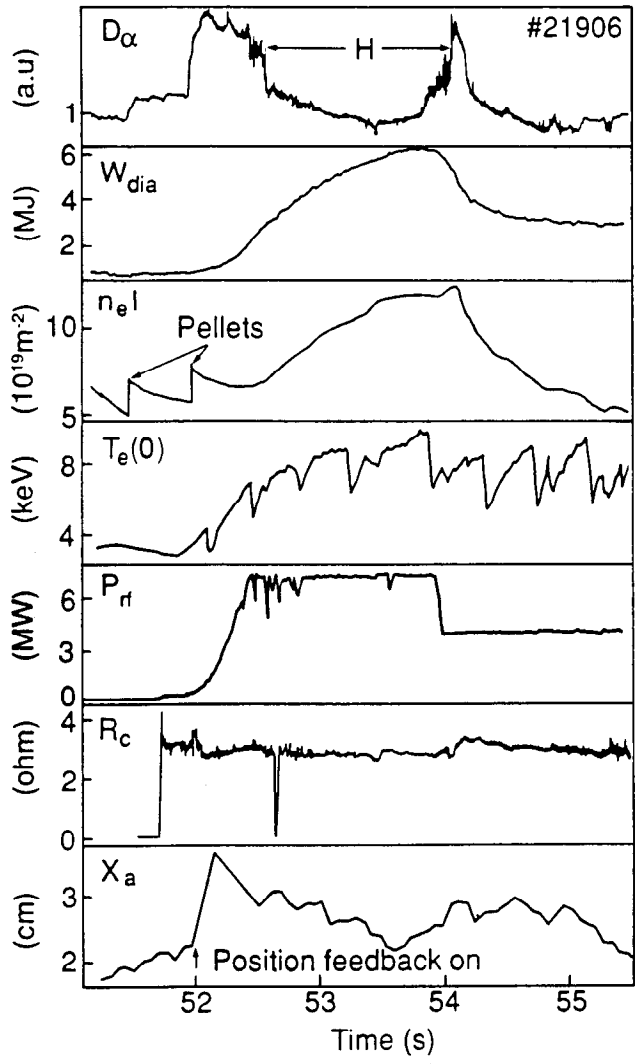

Fig. 6.4. H mode achieved on JET with 7 MW of ICRH alone.[2]

when the central density has risen to 3.7×10^{19} m^{-3} and the energy content given by the diamagnetic loop has reached 6 MJ. In these H modes, the confinement time of the thermal component is about twice the L-mode value and is similar to values obtained with neutral injection at the same power level. Note that by feedback control of the frequency and plasma position, the loading resistance is held constant even during L-to-H and H-to-L mode transitions. By use of beryllium gettering of the machine and using solid beryllium as the Faraday shield material, impurity problems directly associated with ICRF heating have been eliminated. With respect to impurity behavior, density limits and characteristics of the H mode, ICRF heating is essentially indistinguishable from neutral beam injection. Another beneficial effect of ICRF power is the stabilization of sawteeth. Sawtooth-free periods have been produced for up to 3 s in both deuterium and helium plasmas with either hydrogen or ^{3}He minority heating.

Ion cyclotron resonance frequency heating has been used on TFTR to successfully heat plasmas with densities approaching that required of BPX (Ref. 3). Figure 6.5 shows time traces of ^{3}He minority heating of a pellet-fueled discharge with 4 MW of ICRF power. From the initial central electron temperature of $T_e(0) = 700$ eV at $n_e(0) = 2.5 \times 10^{20}$ m^{-3}, the temperature rises to >5 keV while the peak density stays above $n_e(0) = 1 \times 10^{20}$ cm^{-3}. The rapid rise in $T_e(0)$ indicates that there is efficient central power deposition at a density of $n_e(0) = 2.5 \times 10^{20}$ m^{-3}. TFTR has also been very successful in eliminating ICRF-specific impurities by use of boron and carbon as the wall coating and Faraday shield material rather than beryllium.

Many important ICRF heating results have come from other tokamaks. There have been significant high-power ICRF programs on PLT, JT-60, TFR, ASDEX, TEXTOR, TORE Supra, JIPP-IIU, and JFT-2M. A great many heating scenarios have been studied, and various antenna and RF system designs have been employed. Although not all experiments have observed all phenomena (for example, the H mode), the picture of ICRF heating behavior is quite consistent among the various devices.

Observations of ICRF effects in tokamak experiments are in broad agreement with theoretical calculations, although accurate quantitative comparisons are often difficult because of the indirect nature of many of the RF-relevant measurements and because of the tight, nonlinear coupling between the wave launching, wave propagation, tail formation, and energy confinement processes. Theoretical predictions of peaked power deposition profiles are borne out by local measurements with modulated RF power waveforms.[4] Predictions of direct [transit time magnetic pumping (TTMP), electron Landau damping (ELD) mode conversion] electron heating as compared to indirect (tail slowing down) electron heating are confirmed by experiment. Observed reactivity enhancement, due to energetic tail formation, can be modeled with reasonable accuracy.[5] Calculated values of antenna loading resistance are in good agreement with measurements in cases where reasonably accurate measurements of edge plasma density profiles are available.

VI.B.3. Special Heating Scenarios

Although they are not system requirements, additional RF scenarios can be employed for special purposes:

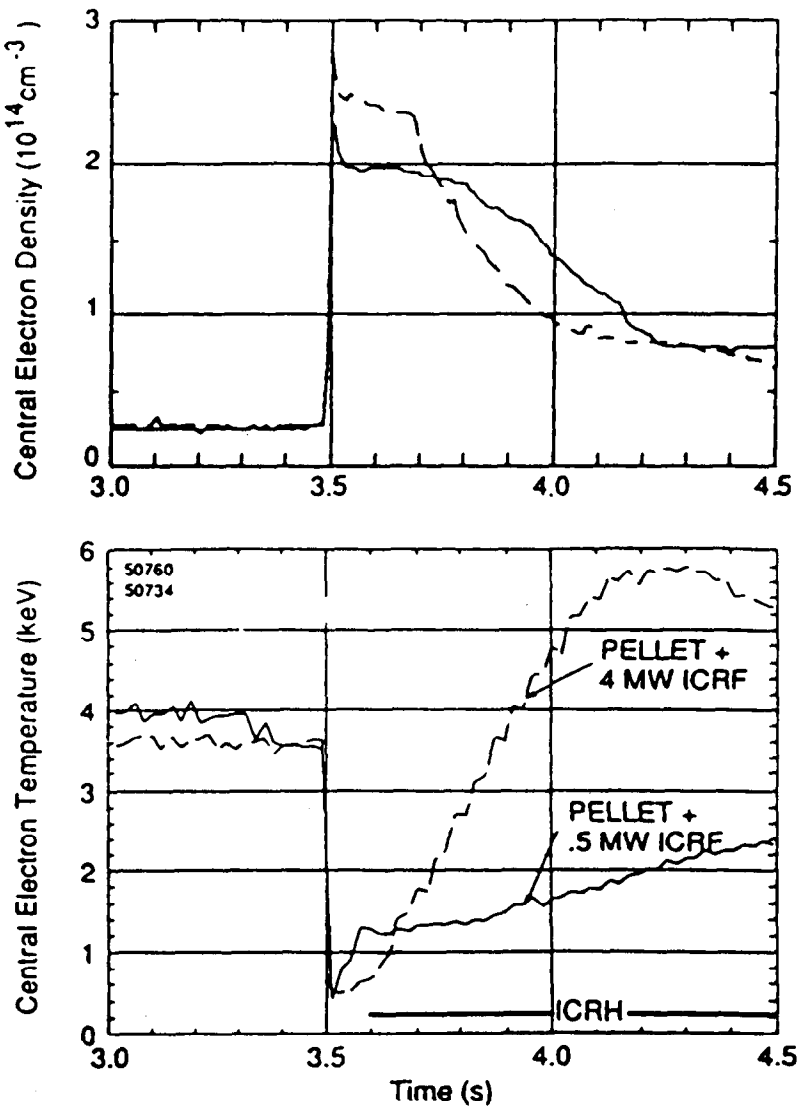

Fig. 6.5. Pellet-fueled density evolution and electron reheat with 4 and 0.5 MW of ICRF power. [D(^{3}He), $B_0 = 5$ T, $I_P = 1.4$ MA] (from Ref. 3).

1. **Off-Axis Heating:** Because of limited flattop time for the plasma current and toroidal field, it may be necessary to begin heating during the B_T ramp. In order to avoid generation of energetic ions in the plasma edge, a requirement is that before the ICRF power is applied, the magnetic field must reach a value such that the hydrogen fundamental resonance be outside the plasma (it may actually be necessary that the resonance be outside the vacuum vessel). If, for example, the scenario is to reach a Shafranov shift of 20 cm, $f_{RF} = 85$ MHz, the hydrogen fundamental resonance leaves the plasma ($R_{edge} = 3.38$ m) when $B_0 > 7.3$ T. Under the same conditions, the resonance leaves the vacuum vessel when $B_0 > 8$ T. In earlier transport simulations, it was assumed that the RF power is applied when $B_0 = 7.6$ T, which places the hydrogen resonance behind the antenna current strap but still inside the vacuum vessel. At this field, the ^{3}He minority resonance occurs at $R = 2.36$ m or inboard of the machine center ($R = 2.59$ m) by about one-third of the minor radius. The heating efficiency will be reduced due to low initial density and temperature and because the resonance is off-axis. In addition, as B_T increases, the fundamental deuterium resonance appears on the inside edge of the plasma. It is conceivable that a difficulty would arise due to the shear Alfvén resonance at the very edge of the plasma, although this has not been observed on other experiments. With the slow toroidal field (TF) ramp currently envisioned, B_T reaches 90% of its flattop value (i.e., 8.1 T) by the time auxiliary heating is applied (typically 4.5 s after plasma breakdown), so this will not be a serious issue. Off-axis heating is important for reasons of flexibility, however, and therefore, it is an item of the R&D plan indicated for further study.

2. **High-Frequency Operation:** Depending on the RF circuit design, it may be possible to operate at reduced power in the frequency range $f_{RF} = 127$ to 137 MHz. This would permit hydrogen minority or deuterium second-harmonic heating at full field. The principle advantage of this mode is that single-pass absorption, even for very small hydrogen minority concentrations, is essentially complete, resulting in a more peaked heat deposition profile and reduced fuel dilution effect compared to ^{3}He minority. Also, the stronger energetic tail produced with H minority is more favorable for sawtooth stabilization.

3. **Preactivation Scenarios:** A preliminary operational phase is planned in which nuclear activation of the device is to be avoided. During this phase, use of deuterium will not be allowed in high-power auxiliary-heated discharges (see Chap. XII). Two ICRF scenarios are possible for this phase: ^{3}He minority in hydrogen majority or ^{3}He minority in ^{4}He majority. As far as the ICRF physics is concerned, the latter is indistinguishable from the very commonly used D(^{3}He) scenario. The H(^{3}He) case is somewhat more complicated. The ^{3}He minority, being the heavier species, is cyclotron resonant on the high-field side of the ion-ion hybrid resonance. The fast wave, propagating from the low-field side, first encounters the fast-wave cutoff, then the hybrid resonance, and finally the ^{3}He cyclotron layer. In order to heat the minority species, the minority concentration must be kept quite low, so that the three singular layers are close together. At higher concentrations, the hybrid resonance moves away from the cyclotron resonance so that only mode conversion to Bernstein waves occurs, resulting primarily in electron heating. In BPX, even concentrations of a few percent ^{3}He are sufficient to move the fast-wave cutoff far away from the resonance and increase the wave reflection. The presence of a deuterium minority in this case would result in strong edge heating, but since deuterium will not have been introduced into the machine, this should not be a problem. Quantitative evaluations of the conditions necessary to achieve good heating in this scenario are ongoing.

   Successful heating experiments were carried out on PLT with heavy minority species,[6] in particular deuterium minority in hydrogen or ^{3}He. The observations were quite consistent with the picture above. No enhanced neutron production or energetic deuteron tail formation was observed with $\eta_D \simeq 10\%$. However, a small decrease in η_D to $\simeq 5\%$ resulted in significant neutrons and an observable minority tail.

4. **Fast-Wave Current Drive:** The TF and poloidal field (PF) systems are capable of pulses up to 45 s at lower field (two-thirds or one-half of the maximum B_T). The divertor system should also be capable of long pulses with alpha power small but still comparable to the auxiliary power. Under such circumstances, interesting experiments are possible when studying fast-wave current drive in D-T plasmas or using fast-wave current drive to modify the current profile for confinement op-

timization. The most promising technique in this regard is to drive electron currents directly with the fast waves by means of transit time magnetic pumping (TTMP) and electron Landau damping (ELD) while attempting to minimize coupling to fuel ions, hydrogen impurity ions, and energetic alpha particles. Figure 6.6 shows the variation of cyclotron resonance frequency for various species across the plasma cross section for $B_0 = 4.5$ T. One scenario that has been considered is to operate in the window just above $f_{RF} \simeq 100$ MHz, which avoids hydrogen fundamental (second-harmonic deuterium, third-harmonic tritium) and hydrogen second-harmonic (fourth-harmonic deuterium). The only ion resonances present are third-harmonic deuterium, alpha, and fourth-harmonic tritium.

If we assume low-density operation [$(n_e(0) \sim 0.5 \times 10^{14}$ cm^{-3})], high electron temperature [$T_e(0) \sim 20$ keV], and low $Z_{eff} \leq 2$, the basic theoretical current drive efficiency is quite high for BPX. Neglecting trapped particle effects, the Fisch-Boozer expression for driven current is

$$I_{RF}(\text{MA}) = 1.6 \times 10^{-3} \frac{T_e(\text{keV})}{n_e/10^{20}} \frac{1}{R} \frac{\tilde{j}}{\tilde{p}} P_{RF}(\text{MW}),$$

where $\tilde{j}/\tilde{p}$ is the normalized current drive efficiency, which depends on $u = v_{\text{phase}}/v_{te}$ and Z_{eff}. For fast waves, where the damping mechanism is predominantly TTMP, and assuming $u \sim 1.5$, which gives strong damping, one finds that $\tilde{j}/\tilde{p} \sim 20$. With the plasma parameters assumed above, we get $I_{RF} \simeq 0.49 P_{RF}$. This expression does not account for the efficiency of depositing the power in the electrons at the proper $v_\parallel$ nor does it include trapped particle effects. A two-dimensional full-wave calculation with the ORION code, which included trapped-particle effects but did not include damping by alpha particles, gave $I_{RF} \simeq 0.36 P_{RF}$ for a single toroidal mode with no upshift in $n_\parallel$.

A preliminary ray-tracing calculation that included a self-consistent alpha-particle profile and did include alpha damping and toroidal upshift of $n_\parallel$ gave much more modest efficiencies with ≃45% of the fast-wave power absorbed by alpha particles at their third-harmonic cyclotron resonance. The calculations were carried out on a ray-tracing code, RAYFAS (Ref. 7), which utilizes an approximate magnetohydrodynamic (MHD) equilibrium flux surface geometry.

To optimize the current drive efficiency, fast waves were launched into a low-density plasma from the midplane on the low-field edge with the following parameters: $n_e(0) = 5 \times 10^{13}$ cm^{-3}, $T_e(0) = T_i(0) = 20$ keV, $B_0 = 4.5$ T, $f = 108.5$ MHz, $k_{T0} = 5.8$ to 11.6 m^{-1}, with a 50/50 D-T plasma mixture. The frequency was chosen to minimize alpha absorption, by placing the fourth-harmonic alpha resonance on the outboard edge ($R = 3.36$ m) and the third-harmonic resonance on the high-field side ($R = 2.50$ m) of the magnetic axis ($R = 2.79$ m). Given the $T_i(= T_e)$ and n_i profiles, the self-consistent fast alpha density profile is calculated. The various damping decrements are evaluated, including that of the energetic alphas, using a slowing-down distribution function that scales as v^{-3}. To calculate the driven current, a normalized efficiency scaling taking into account trapped electron and TTMP effects has been used.

The calculated fast alpha concentration n_α/n_e has a peak value of 0.6%. A single ray with launch point 0.2 m below the midplane is used with an incident toroidal wave number of 5.8 m^{-1}. Only single-pass absorption was considered, which in this case results in 56% of the incident power absorbed in one radial transit. Figure 6.7 shows power absorption profiles for electrons, fuel ions, and alpha particles. The increase in $k_\parallel$ as the ray propagates inward results in the broadening of the Doppler width of the third alpha harmonic, resulting in a broad alpha absorption profile. Electrons absorb about 42% of the total absorbed power, with alphas and tritons accounting for 45 and 13%, respectively. As a result, the current drive effi-

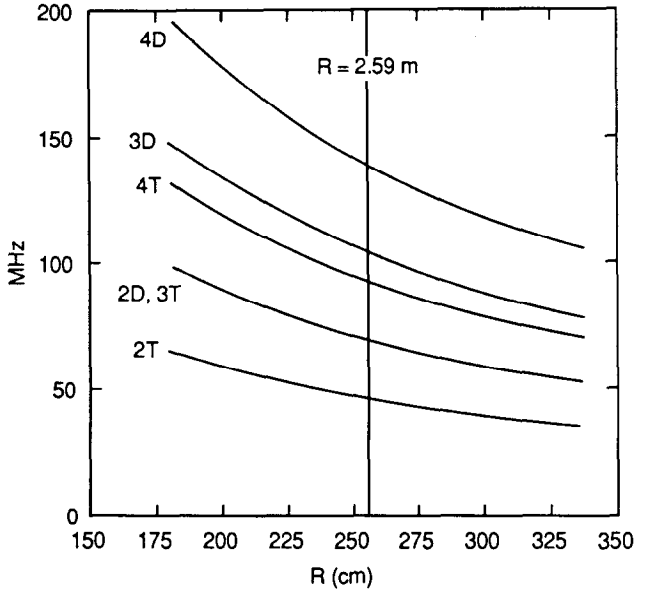

Fig. 6.6. Cyclotron frequency of various plasma species versus major radius, $B_0 = 4.5$ T.

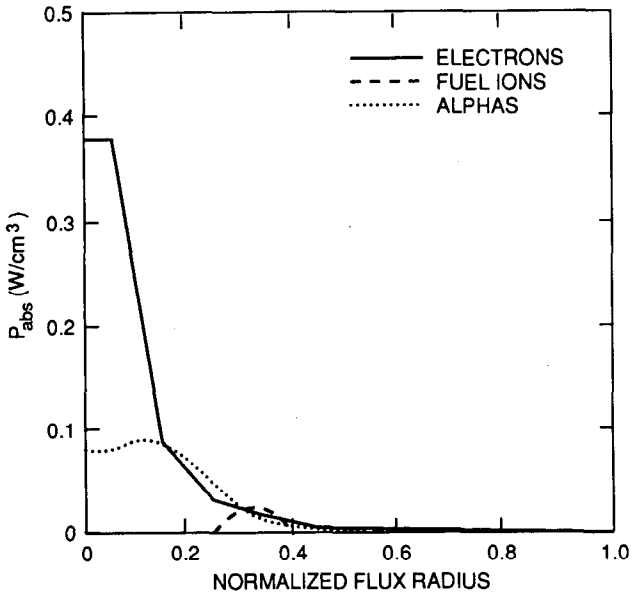

Fig. 6.7. Power deposition in various species versus radius.

ciency is 0.154 A/W if subsequent passes have similar efficiency.

A second case has also been studied in which the incident wave number is doubled to 11.6 m^{-1} in order to increase the fraction of electron absorbed power. The results indicate a 66, 32, and 2% distribution of absorbed power among electrons, alphas, and tritons, respectively. However, the current drive efficiency is slightly degraded to 0.151 A/W, probably because the wave interacts with a larger proportion of thermal electrons.

The most important factor that could further reduce current drive efficiency is the directivity of the antenna array. Further study is needed to determine whether the proposed antenna array can produce an adequate $k_\parallel$ spectrum and whether a frequency range can be found that permits efficient coupling to electrons without parasitic heating of the fuel ions or alpha particles. Another possibility is to use a low-frequency scenario similar to that proposed for ITER with $f_{RF} \simeq 50$ MHz. This avoids the fundamental deuterium, alpha, and fundamental hydrogen (second-harmonic deuterium, alpha) resonances but has reduced electron absorption and more difficult $k_\parallel$ spectral control. More extensive evaluation of the feasibility of fast-wave current drive will be carried out as a part of the BPX R&D program.

VI.B.4. Single-Pass Absorption

An indication of the power deposition in a given heating scenario can be obtained by considering the transmission, reflection, absorption, and mode conversion at the resonance layer. To do this, one solves a sixth-order full-wave equation that describes fast and slow ion cyclotron waves, as well as Bernstein waves up to second harmonic.[8] A number of codes have been developed for this purpose (see references contained in Ref. 8). Many of these codes have been benchmarked against each other and are known to give good agreement. The geometry is a slab with magnetic field, density, and temperature variations in the x direction, **B** in the z direction, and $k_\parallel$ = const as the wave propagates. Figure 6.8 shows the dependence of the various coefficients as a function of $k_\parallel$ for the full-field ^{3}He case with $\eta_{^3He} = 1.5\%$. The plasma parameters are representative of the ohmic startup phase with moderate density, $n_e(0) = 2.5 \times 10^{20}$ m^{-3}, and low temperature, $T_e = T_i = 3$ keV. We have taken $B(0) = 8.48$ T ($f_{RF} = 86.2$ MHz). For the present baseline antenna design (hybrid antenna, described in Sec. VI.B) with dipole phasing (0, π), the peak of the radiated $k_\parallel$ spectrum occurs at about 10 m^{-1}. One can see that at this $k_\parallel$, about 60% of the power is dissipated in the various plasma species or is mode converted (to be dissipated primarily by electrons), whereas about 10% is reflected back toward the antenna and 30% is transmitted to the high-field side. The power reflected or transmitted will be rereflected back into the plasma center from the plasma edge, ex-

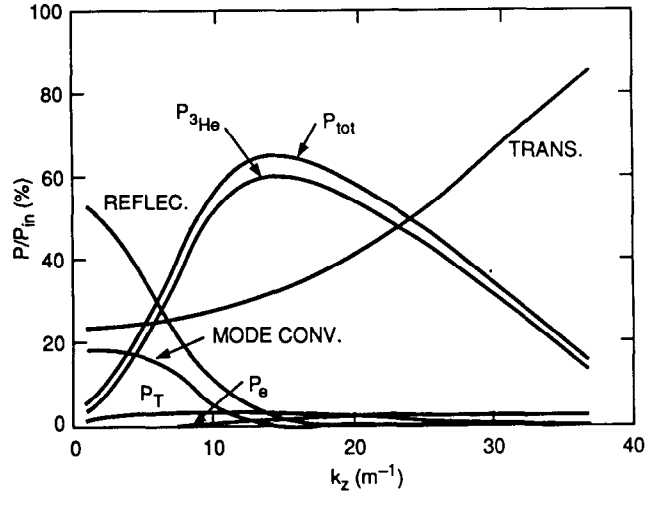

Fig. 6.8. Wave scattering coefficients for BPX D-T(^{3}He): $B_0 = 9$ T operation at low startup temperature ($T_e = T_i = 3$ keV) and $\eta_{^3He} = 1.5\%$.

cept that a portion of the transmitted power might be absorbed at the edge by the shear Alfvén resonance. With $(0, \pi)$ phasing of the current straps, very little power resides in $k_{\|}$ components below 5 m^{-1}. With monopole phasing (0, 0), reflection and transmission are dominant, mode conversion being the most significant absorption process. In experiments with monopole phasing, density-dependent resonant peaks are observed in the antenna loading associated with standing waves between the plasma edge and the cutoff layer. Also, impurity generation has been seen to be more of a problem with monopole phasing.[9]

Figure 6.9 shows the dependence of the various coefficients as a function of $k_{\|}$ for the 2/3 field ^{3}He case with $\eta_{^3He} = 1.0\%$, $n_e(0) = 2.5 \times 10^{20}$ m^{-3}, $T_e = T_i = 3$ keV, and $B(0) = 5.66$ T ($f_{RF} = 57.5$ MHz). Here the absorbed power is even greater and the reflected power is much less, due to the smaller minority concentration and greater tunneling coefficient.

The equivalent 2/3 field case for minority hydrogen ($\eta_H = 1.0\%$) is shown in Fig. 6.10. Here absorption is nearly complete for $k_{\|} > 5$ m^{-1}. These results are consistent with previous calculations done for earlier versions of the design having higher B field and smaller R_0.

In order to give an indication that this degree of one-pass absorption is indeed sufficient, in Fig. 6.11 we provide scattering coefficients for the experimental data from TFTR shown in Fig. 6.5. The plasma parameters used were for the time $t = 3.75$ s, $n_e(0) = 2.0 \times 10^{20}$ m^{-3}, $T_e = T_i = 2$ keV, $B(0) = 5.0$ T ($f_{RF} = 50.8$ MHz), and $\eta_{^3He} =$ 2.0%. Although the theoretically predicted maximum power dissipation was only about 45% and the transmission was greater than 50%, excellent heating with no enhanced impurity influx was observed in the experiment.

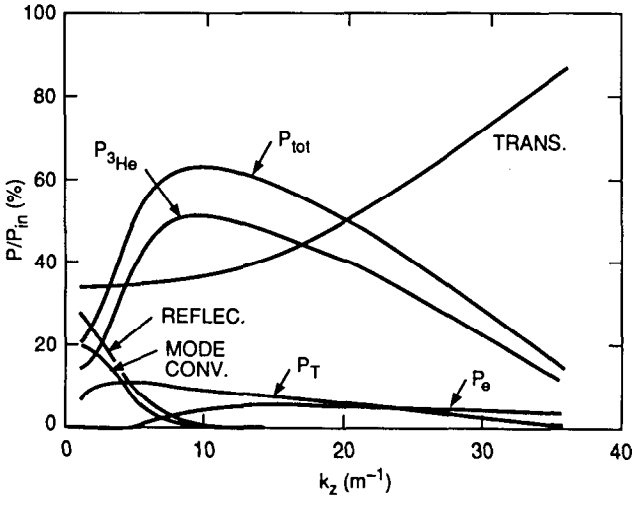

Fig. 6.9. Wave scattering coefficients for BPX D-T(^{3}He), $B_0 = 6$ T operation at low startup temperature ($T_e = T_i = 3$ keV) and $\eta_{^3He} = 1.0\%$.

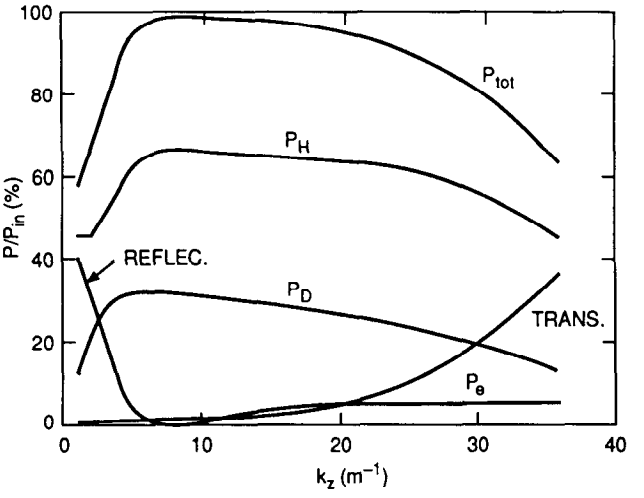

Fig. 6.10. Wave scattering coefficients for BPX $DT(H)$, $B_0 = 6$ T operation at low startup temperature $T_e = T_i = 3$ keV, $\eta_H = 1.0\%$.

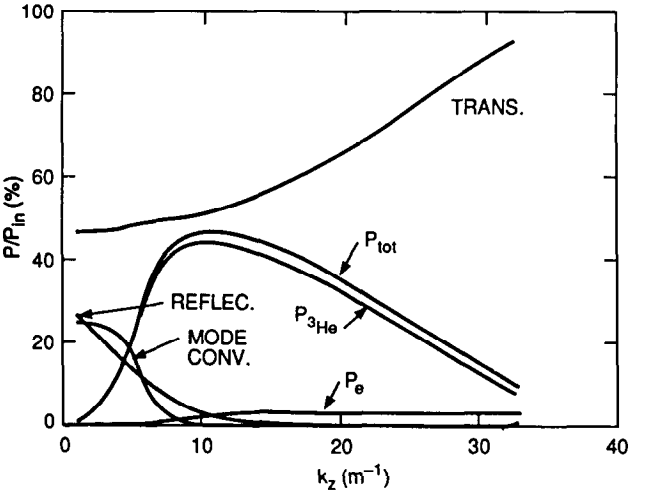

Fig. 6.11. Wave scattering coefficients for TFTR D(^{3}He): $B_0 = 5$ T, $n_e(0) = 2.0 \times 10^{20}$ m^{-3}, $T_e = T_i = 2$ keV, and $\eta_{^3He} = 1.0\%$.

These results are sensitively dependent on the concentration of the minority species η_{min}. At very low values of η_{min}, damping by the minority is small, and most power is transmitted through the resonance layer. At large values of η_{min}, the evanescent region between the fast-wave cutoff and the ion-ion hybrid layer increases so that reflection is larger, minority cyclotron damping is weak,

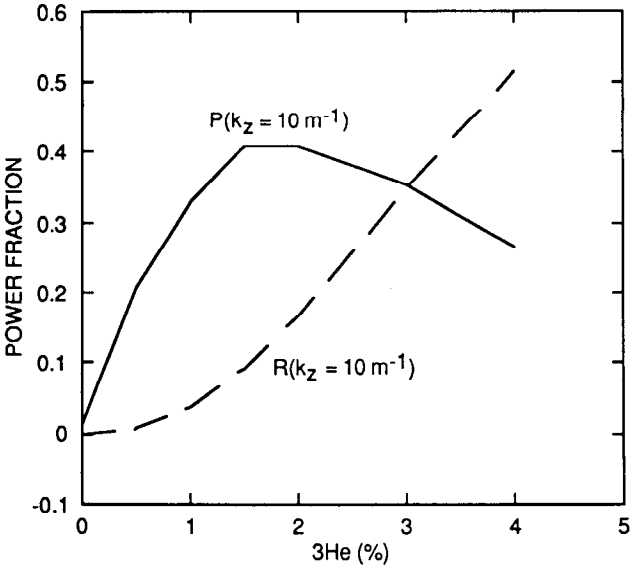

Fig. 6.12. Power fraction absorbed + mode converted (solid) and power fraction reflected (dashed) versus η_{3He}, $n_e(0) = 1 \times 10^{20}$ m^{-3}, $T_e = T_i = 3$ keV, $k_{\|} = 10$ m^{-1}.

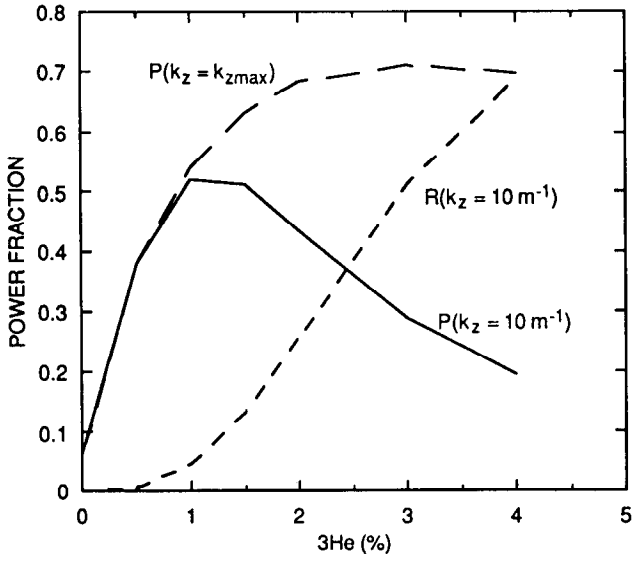

Fig. 6.13. Power fraction absorbed + mode converted (solid), power fraction reflected (dashed), versus η_{3He}: for $k_{\|} = 10$ m^{-1}, and power fraction absorbed + mode converted for $k_{\|}$ value having maximum absorption: $n_e(0) = 2.5 \times 10^{20}$ m^{-3} and $T_e = T_i = 3$ keV.

and mode conversion becomes the dominant absorption process. Large values of η_{min} are also undesirable from the standpoint of fuel dilution. There is an optimum concentration that maximizes single-pass absorbed power with acceptable fuel dilution. Figure 6.12 shows a plot of total power absorbed by the plasma (absorbed + mode converted) at $k_{\|} = 10$ m^{-1} as a function of η_{3He} for a relatively low-density [$(n_e(0) = 1 \times 10^{14}$ cm^{-3})], low-temperature [$(T_e(0) = T_i(0) = 3$ keV)] startup plasma. We see that the optimum concentration is about $\eta_{3He} = 1.7\%$ and that reflected power at this concentration is $\simeq$12%, an acceptable value. At higher plasma density, the peak shifts to lower minority concentration. Figure 6.13 shows a case similar to Fig. 6.12 but for $n_e(0) = 2.5 \times 10^{20}$ m^{-3}. Here the optimum concentration is about 1% with reflected power $\simeq$ 4%. Also shown in this figure is the absorbed power for the value of $k_{\|}$ having maximum absorption for given η_{3He}. We therefore anticipate operation with ^{3}He concentration in the vicinity of 1%. Based on the TFTR results, one could conclude that even lower concentrations are adequate to provide sufficient damping, if required to minimize fuel dilution.

The presence of the poloidal field tends to modify the picture afforded by these simple slab calculations. Since there is actually a nonzero component of B in the direction of the magnetic field gradient, $k_{\|}$ is not constant as the wave propagates nor are particle parallel velocities constant. The problem is therefore nonlocal and is not separable by a simple Fourier transformation along the magnetic field. This problem has been studied in several recent calculations that include the poloidal field and nonlocal aspects directly in the formulation of the conductivity tensor operator.[10] The result is that reflection and mode conversion tend to be reduced as compared to the simple slab, while cyclotron absorption is increased. These effects are particularly important at low $k_{\|}$, where reflection appears dominant.

VI.B.5. Two-Dimensional Full-Wave Calculations

The scattering coefficients do give an indication of the relative strengths of the absorption processes and of the importance of reflection and mode conversion, but in practice, the mode-converted wave is damped (primarily by electrons), and the transmitted and reflected waves propagate to the plasma surface where they are re-reflected back into the plasma. Also the absorption must be summed over the $k_{\|}$ (or toroidal mode number N_T) spectrum excited by the antenna. These effects can be properly included in a two-dimensional full-wave code. Fig-

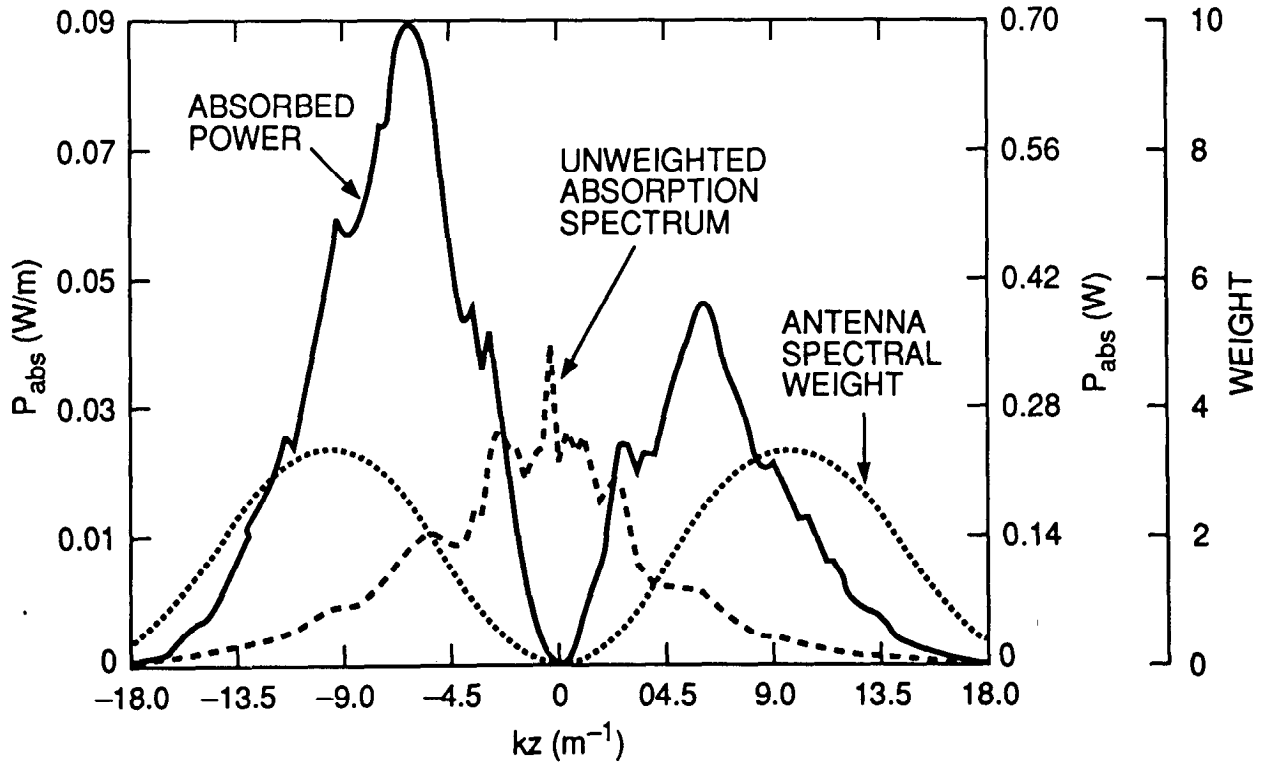

Fig. 6.14. ORION calculation of power absorption spectrum for nominal ^{3}He operation.

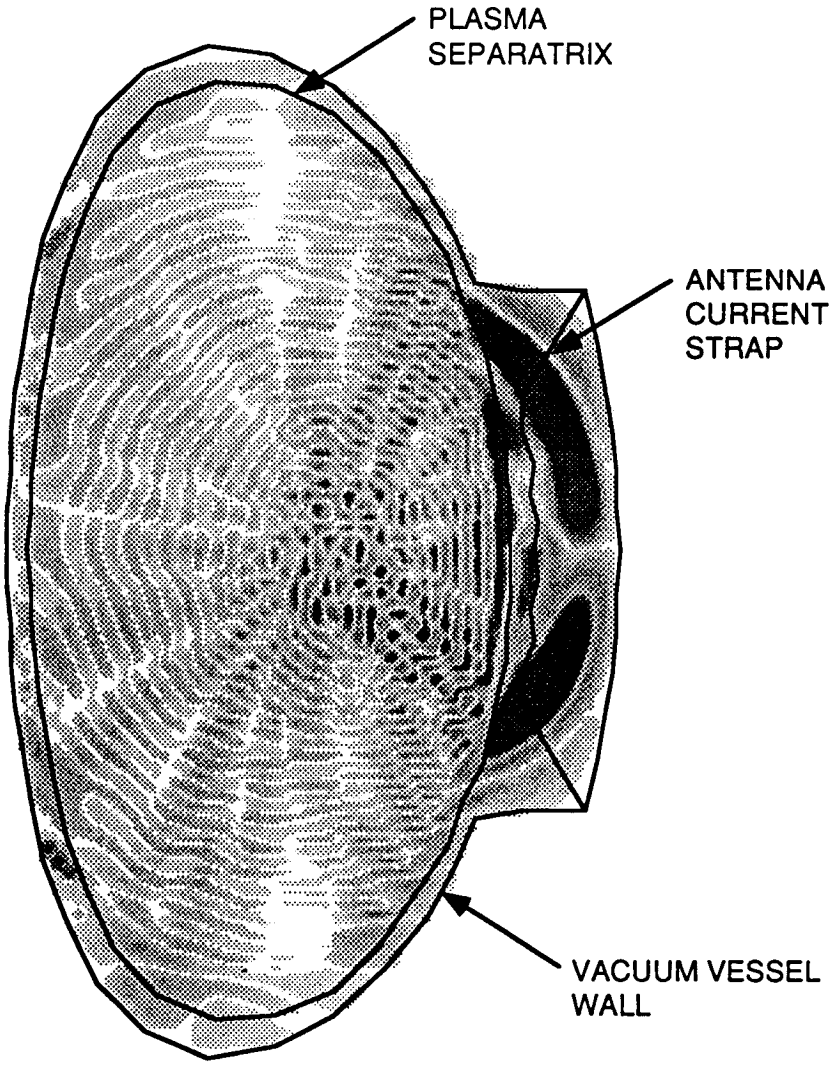

Fig. 6.15. Gray-scale density plot $\mathrm{Re}\{E_{y(x,y)}\}$ for the case shown in Fig. 6.14.

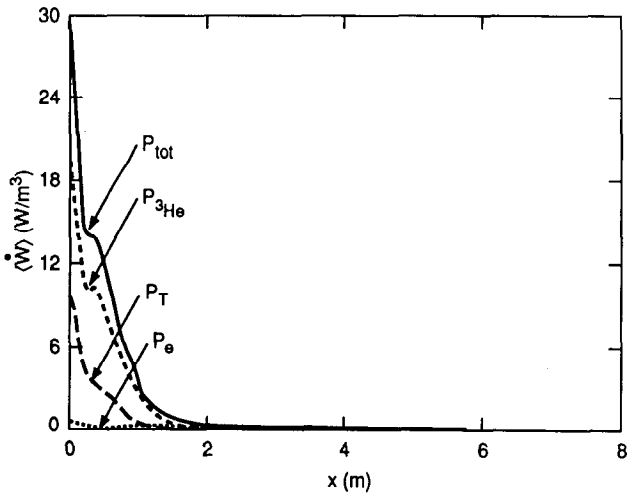

Fig. 6.16. Flux surface average of power deposition versus distance from magnetic axis.

ures 6.14, 6.15, and 6.16 show results for BPX obtained with the ORION two-dimensional full-wave code.[11]

The antenna was assumed to consist of two current straps of toroidal width 14.6 cm, separated by 30.5 cm center to center and located 30 cm radially in from the back conducting wall. The straps were driven out of phase $(0, \pi)$. This is consistent with the design of the BPX "hybrid" antenna described in more detail in Sec. VI.C. The plasma parameters were $\langle n_e \rangle = 2.5 \times 10^{20}$ m^{-3}, $T_e(0) = T_D(0) = T_T(0) = 14$ keV, and $T_{3_{He}} = 100$ keV with 1.5% ^{3}He in a 50-50 D-T mixture. A flat density profile with a steep linear drop at the edge was used. A total of 101 toroidal modes were included in the calculation, summed from $N_T = -50$ to $+50$. Figure 6.14 shows the N_T spectrum of the antenna current density (dotted line), the un-normalized power absorption spectrum (dashed line), and the power absorption spectrum weighted by the antenna current density spectrum (solid line). The antenna spectrum peaks at about 10 m^{-1} and is very small near $N_T = 0$, where, as seen from the previous scattering coefficient figures, reflection and mode conversion dominate. Figure 6.15 shows a gray-scale density plot of $\mathrm{Re}\{E_y\}$ in a poloidal cross section. One can see that the wave energy is tightly focused toward the center, and very little RF field actually penetrates to the high-field side of the resonance. Figure 6.16 shows the radial profile of wave power absorption for the various species. This is indeed highly peaked near the magnetic axis. Of the total absorbed power, 62.25% is absorbed by the ^{3}He minority, 15.95% by the fuel tritium, 0.58% by the deuterium, and 21.2% by electrons.

VI.B.6. Stabilization of Sawteeth

An important aspect of ICRF heating pertaining to plasma performance is the creation of a hot banana-trapped ion tail and its inherent stabilization properties. The existence of a trapped hot ion component has been shown theoretically to stabilize resistive and ideal low-n internal kink modes.[12,13] A key criterion for this stabilization is that the precession frequency of the hot ions exceeds the growth rate of the MHD mode; large precession frequencies (high temperatures) are characteristic of ICRF-produced tails. While theory has shown that sawteeth can be stabilized by these hot particles at modest values of β_{hot}, too great a hot ion component can destabilize fishbones.

Sawtooth stabilization has been observed experimentally in a number of tokamaks with different heating methods. In TEXTOR neutral-beam-injected discharges, the sawtooth period was observed to increase with increasing hot ion beta.[14] ICRF-only JET discharges revealed sawteeth suppressed for periods of up to 5 s (Ref. 15). The most effective suppression of sawteeth was found when the ICRF was injected early in the discharge during current rampup, when r_{inv}/a was small. In fact, the period of sawtooth suppression lasted for as long as it took for the current profile to reach a near-steady-state value. ICRF sawtooth stabilization has also been observed on TFTR (Ref. 16) with properties similar to those observed on JET (Ref. 17). Analysis of the JET and TFTR data indicates that the sawtooth-free discharges lie approximately within the stabilized regime as determined by the ideal limit of the hot ion stabilization theory.

The ability to stabilize sawteeth in BPX will depend critically on the energies and distribution of the hot ion population (either the hot ion tail produced by ICRF heating or the alpha population). A study to evaluate these effects is currently under way. Preliminary calculations suggest that tail temperatures of hundreds of keV will be needed to stabilize sawteeth in BPX. Such tails can be generated in the central region of the plasma ($r < 0.15$ m), at moderate densities, with sufficiently peaked RF heating.

VI.B.7. Summary of ICRF Physics

ICRF heating is a well-established technique that has been successful on many tokamaks. The heating scenarios planned for BPX (^{3}He and hydrogen minority) are commonly used on existing

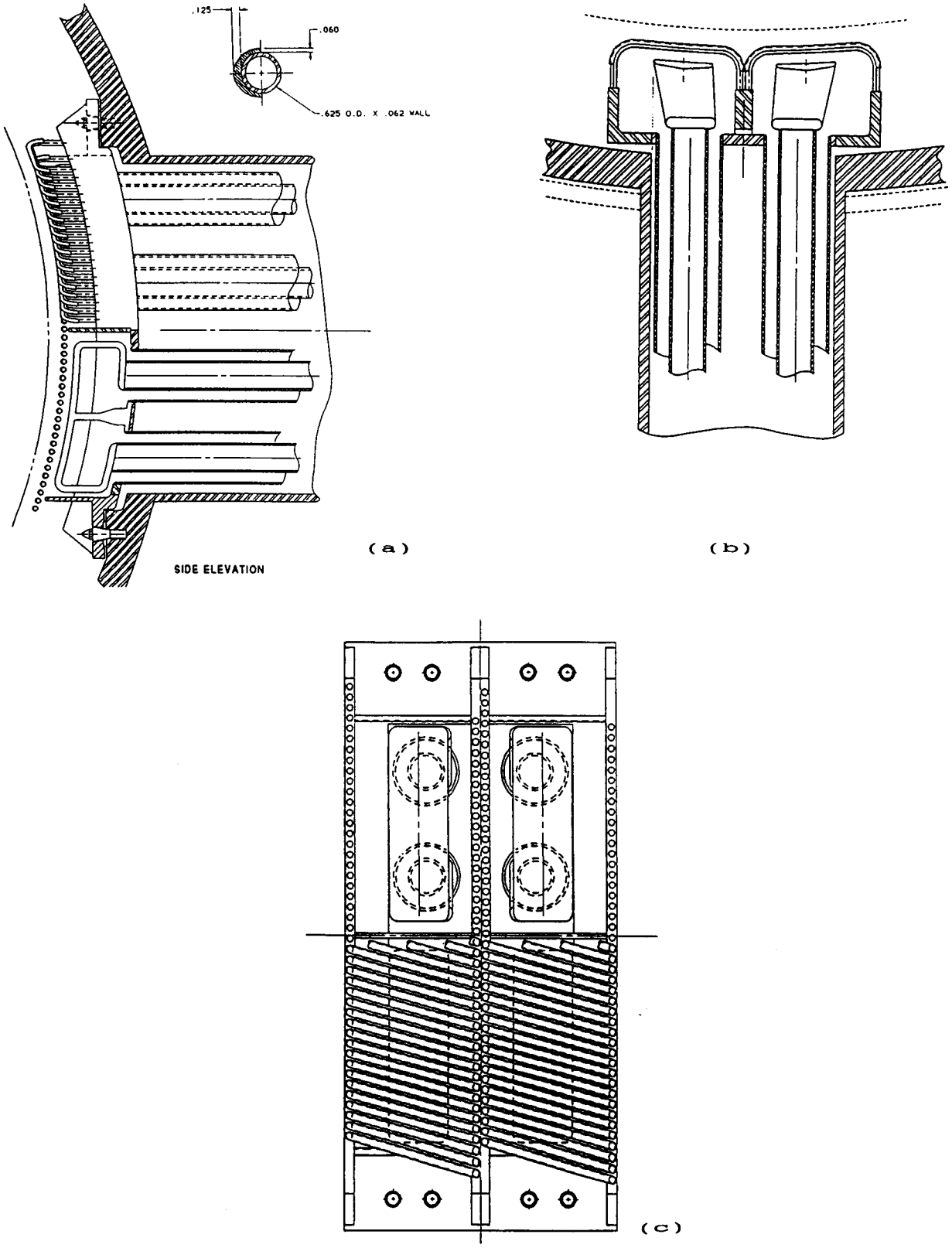

Fig. 6.17. BPX hybrid antenna: (a) side elevation, (b) plan view, and (c) front view.

tokamaks. A number of the problems long associated with ICRF have now been resolved. For example, the influx of impurities associated with ICRF on JET and TFTR are not different from those associated with an equivalent amount of neutral beam injection power. Long-lived H modes have been produced, using ICRF alone, whose pulse lengths are limited only by the density influx and associated rise in radiation. These H modes are not different from those produced by other heating methods. Heating at densities approaching that planned for BPX has been achieved on TFTR. All indications from experiment and theory suggest that ICRF can be used successfully to heat BPX.

VI.C. ANTENNA DESIGN ISSUES

Plasma physics considerations impact ICRF antenna design in two primary areas: antenna loading resistance and Faraday shield design. For a given antenna design with specified voltage limits, the power that can be coupled to the plasma per antenna is proportional to the antenna load resistance. This quantity can vary over a wide range, depending on antenna design and details of the plasma density profile. Therefore, considerable effort has been invested in determining the worst-case density profiles, determining loading for these profiles, and investigating the sensitivity of loading to variations around these profiles.

The present antenna design is referred to as the "hybrid" design since each antenna unit, which consists of a 2 × 2 array of current straps, is to be inserted through a port opening, while the Faraday shield assembly, which is larger than the port size, is mounted on the wall from the inside. The rationale for this is to maximize the radiating area of the antenna by permitting the electrically active current strap components to fill the port area. This optimizes the $k_{\|}$ spectrum within the limitations of port size but allows the electrical assembly to be removed through the port for ease of remote maintenance. The engineering difficulties of any ICRF antenna design for a device such as BPX are significant. These are discussed in detail in the System Design Description. Figures 6.17a, 6.17b, and 6.17c show, respectively, side elevation, front elevation, and plan views of the hybrid design. Each of the four current straps is shorted to ground at the center and driven by coaxial transmission lines at each end (eight feed connections per antenna). To achieve 20-MW total power to the plasma, four such units composed of four straps each will be employed, requiring 1.25 MW per strap.

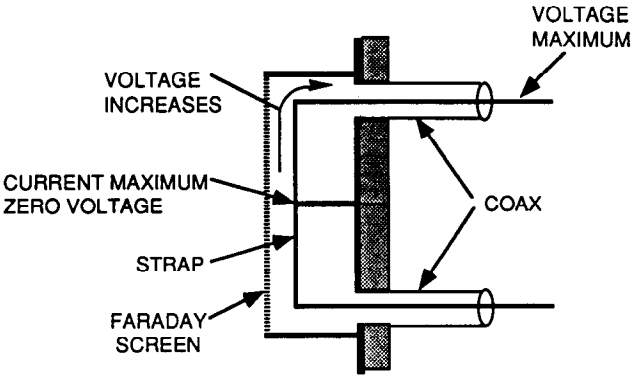

Fig. 6.18. Schematic view of double-end-fed loop antenna.

VI.C.1. Power Handling and Voltage Limits

The limit to the amount of power that can be radiated by a given antenna is found in practice to be determined by a maximum voltage V_{max} that can be applied to the antenna without producing a breakdown at some location in the antenna/transmission line system. This does not correspond to a specific power limit since at V_{max} the radiated power can increase or decrease, depending on how favorable is the coupling to the plasma. The radiated power is proportional to the square of the antenna current, integrated along the length of the current strap:

$$P_{rad} = \frac{1}{2}\int_0^{h_s} dl R'(l) I^2(l),$$

where R' = loading resistance in ohms per meter, h_s = height of current strap, and l is distance along the current strap. R' is determined both by antenna design and by the plasma density profile, particularly the low-density edge profile. I varies along the current strap because of finite phase velocity. The magnitude of I is proportional to the applied voltage and inversely proportional to the characteristic impedance of the strap. The loading resistance typically accounts for only a small part of the antenna input impedance so that an increase in R' translates essentially directly into a proportional increase in radiated power at fixed V.

The distribution of current and voltage on the antenna can be understood by considering it as a leaky strip transmission line, with the Faraday shield acting as a ground plane that adds capacitance but has little effect on the inductance per unit length. This is shown schematically in Fig. 6.18, where, for the BPX design, the strap is shorted to ground at the center and fed at either end. The current maximum is at the short,

Table 6.1. Typical Voltage Limits in Experiments

		Design Voltage	Maximum Operation (w/plasma)	Typical Operation
TFTR	(Bay L)	50	60	50
	(Bay M)	50	50	40
JET		32	28	25
JT-60		50	30[a]	30
DIII-D		50	17[b]	17
BPX		50	50	30 - 35

[a] Administrative limit.
[b] Transmitter power limited.

whereas the voltage is zero there. In moving away from the short, toward either feed point, the current drops and the voltage rises. Figure 6.19 shows a coupled, lossy transmission line model of the RF voltage and current on the current strap and feed transmission line as a function of distance from the center short.[18] The dashed line indicates the junction between the ends of the radiating current strap and the feed system. It can be seen that the voltage maximum occurs at about 0.7 m from the short and, for these particular parameters, is about 33 kV. Since the half-length of the current strap is only about 0.24 m, this maximum voltage point occurs back in the coaxial feeder. The maximum voltage on the current strap itself is 25 kV. This calculation was done for an assumed loading resistance of $R' = 8.9\ \Omega/\text{m}$, which corresponds to the worst-case H-mode density profile at a volume-average density of $\langle n_e \rangle = 5 \times 10^{20}\ \text{m}^{-3}$, the Greenwald limit for BPX (see Fig. 6.30). The loading resistance is further reduced by a factor of 0.92 to account for end effects (discussed in Sec. VI.C.3). After subtracting the RF power dissipated in the current strap and Faraday shield, the radiated power is then 1.25 MW/strap at a peak voltage in the system of 32.5 kV. The peak system design voltage for BPX is to be 50 kV. Table 6.1 shows the design voltages, maximum attained operational voltages, and typical operational voltages for several existing ICRF experiments as well as for BPX. It can be seen that the values for BPX are comparable to those for present experiments. The choice to set the BPX operating conditions to handle worst-case plasma conditions provides a measure of conservatism.

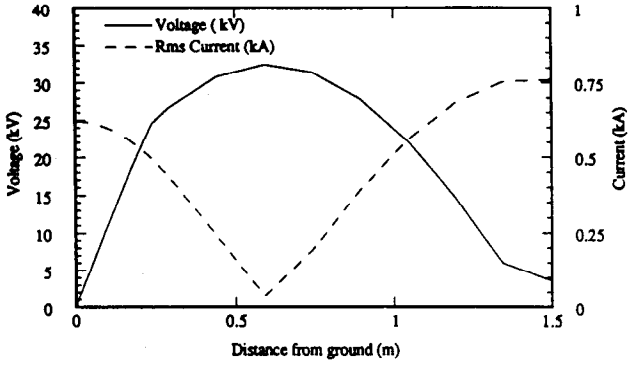

Fig. 6.19. RF voltage (solid line) and current (dashed line) versus distance from short for BPX hybrid antenna.

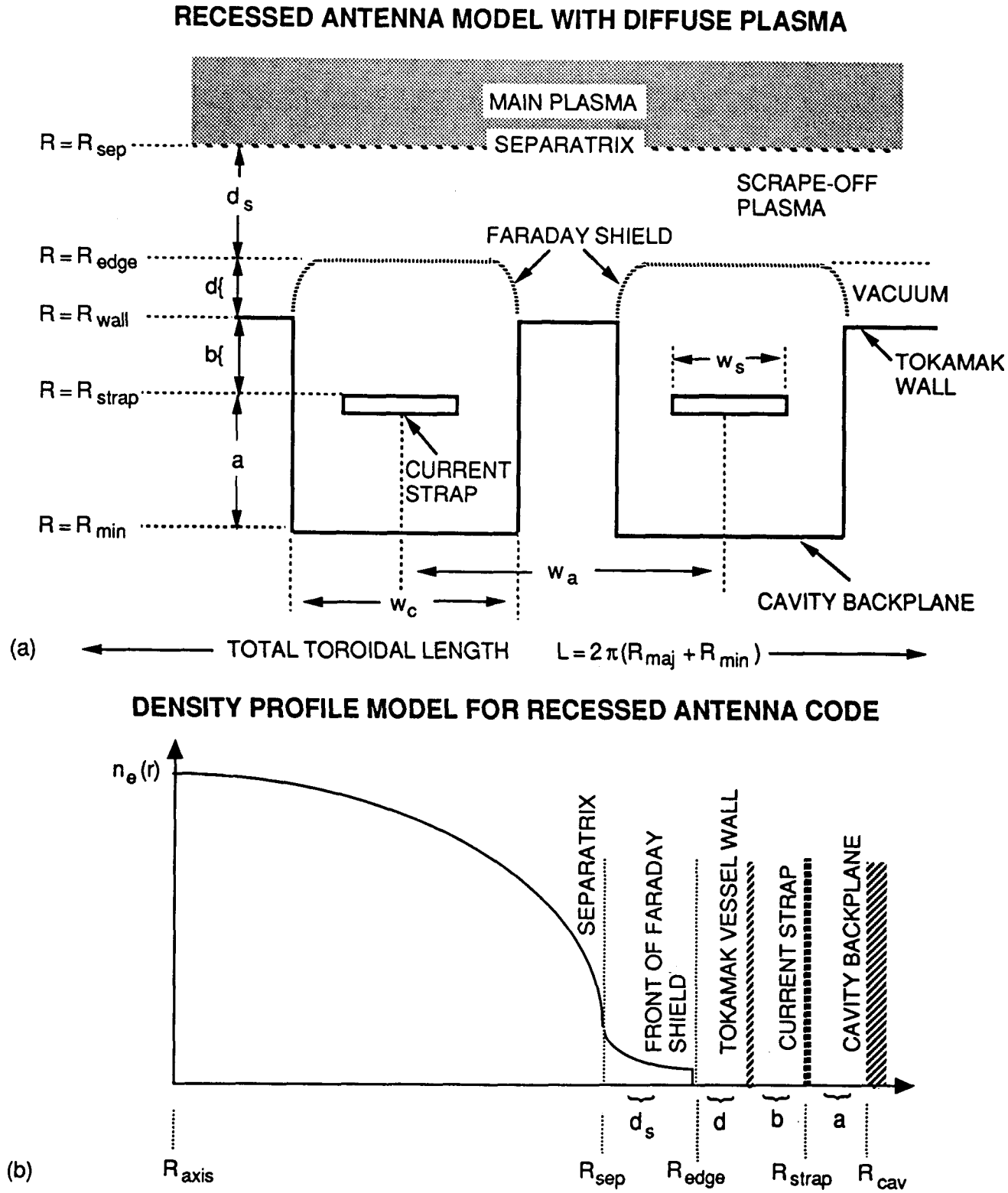

Fig. 6.20. (a) Model geometry and (b) geometric parameters for RANT recessed antenna model.

VI.C.2. Calculation of Antenna Loading

A number of codes exist for computing loading characteristics of current strap antennas facing slab plasmas.[19–21] In order to provide a quantitative basis for evaluation of BPX antenna designs, we have used the Oak Ridge National Laboratory recessed antenna modeling code RANT to perform extensive calculations for a number of different BPX antenna designs (hybrid, port-mount designs, wall-mount designs) for a variety of edge density profiles.

The geometry for the recessed model is shown in Fig. 6.20a. The magnetic field is constant and oriented in the z direction. Two radial-like coordinates are used: R, which is measured out from the magnetic axis, and x, which is measured in from the plasma edge, $x = R_{edge} - R$. The boundary consists of a perfectly conducting wall with an arbitrary number of recesses (two recesses for these calculations). Each recess contains a y-directed current strap (zero thickness in x) of width W_s in z. The plasma, current straps, and boundary are uniform in y (i.e., there is no poloidal variation). The model therefore gives loading per unit length of current strap. The plasma is uniform in z and has arbitrary variation in R (or x) out to $R = R_{edge}$, beyond which the density vanishes. One can visualize this as the location of a Faraday shield or antenna bumper limiter that cuts off the plasma. There is actually no need for a separate Faraday shield model in this code since only transverse electric (TE) fields are included ($\mathbf{B} \parallel$ to $\hat{\mathbf{z}}$ and $\mathbf{J} \parallel$ to $\hat{\mathbf{y}}$). The x variation of the density profile is arbitrary. A density profile that would be appropriate for gas-fueled L-mode plasmas or pellet-fueled H-mode plasmas is shown in Fig. 6.20b, i.e., square-root parabolic out to R_{sep} and exponential from R_{sep} to R_{edge} with a drop to 0 at R_{edge}.

There are four x regions (or equivalently R regions) in which the wave field must be represented:

Region 1

$R_{strap} < R < R_{back}$

vacuum region between strap and cavity backplane, one for each recess

Region 2

$R_{wall} < R < R_{strap}$

vacuum region between tokamak wall and strap, one for each recess

Region 3

$R_{edge} < R < R_{wall}$

vacuum region outside recess between tokamak wall and front of Faraday shield

Region 4

$0 < R < R_{edge}$

plasma region

The field is expanded in terms of the appropriate eigenfunctions for each region. The z distribution of antenna current $\mathbf{J}_y(z)$ is also expanded in the recessed-region eigenfunctions. Because of nonuniformity of the boundary in the z direction, the different Fourier modes in z are coupled. This coupling arises when appropriate matching of the fields and their derivatives is enforced at the junctions of the four regions. We ultimately arrive at a large system of linear equations for the expansion coefficients in region 1 as driven by the expansion coefficients of $\mathbf{J}_y(z)$. These are then used to determine the field amplitudes in the other regions and, by summation, the E_y field and Poynting flux are determined in space.

The time average power flux in the x direction is, in SI units,

$$\begin{aligned} S_x &= \tfrac{1}{2}\mathrm{Re}\{E_y^* H_z\} \\ &= \frac{1}{2\mu_0\omega}\mathrm{Re}\left\{\frac{1}{i}E_y^*\frac{\partial E_y}{\partial x}\right\} \qquad \mathrm{W/m^2}. \end{aligned}$$

Integrating over the z extent of the device, we obtain for the total radiated power per unit length in the y direction

$$\mathrm{P}(x) = \int_0^{h_s} dz \mathrm{S}_x(x,z) \qquad \mathrm{W/m}.$$

For a nondissipative plasma, as is assumed here, $\mathrm{P}(x)$ is actually independent of x and can be evaluated at any convenient location. To obtain a loading resistance per unit length per current strap R', we assume the loading to be uniform along the length of the strap and take

$$\frac{1}{2}R'|I|^2 = \frac{P}{N_A},$$

where N_A is the number of current straps (in this case, 2).

VI.C.3. Benchmarking of Calculated Loading Against Experiments

To have confidence in our ability to predict loading for BPX, it is necessary to compare modeling results with measurements on actual experiments. This is not an easy comparison because loading is sensitive to details of the plasma density immediately in front of the antenna (which is poorly measured except in a few cases) and because corrections for poloidal variations must be made to our

loading per unit length in the y (poloidal) direction. Fortunately, laboratory measurements have been made of the poloidal corrections for some antennas where reasonable information about the edge density is available: a single-strap antenna on DIII-D and the Bay-M and Bay-L antennas on TFTR.

To correct for poloidal field variations, it is convenient to define an effective strap length $(h_s)_{eff}$:

$$(h_s)_{eff} = \frac{1}{B_z^2(\max)} \int_0^{h_s} dl B_z^2(l),$$

where $B_z(\ell)$ is the RF toroidal magnetic field that is produced by the antenna in vacuum as measured just in front of the current strap. Then the load resistance R_L can be defined as

$$R_L = R' \cdot (h_s)_{eff},$$

where R' = uniform load resistance per unit length obtained from the model. The radiated power per strap is then

$$P_{rad} = \frac{1}{2} R_L I_{\max}^2.$$

There are two physical effects that contribute to the variation of B_z along the strap:

1. **Finite phase velocity:** The current wave is a standing wave with peak at the center short. The current varies therefore as $\cos(\kappa y)$ where $\kappa = \lambda / c v_{phase}$.
2. **End effect:** B_z is cancelled by image currents in the antenna wall near the end of the strap. This is a particularly large effect in the DIII-D antenna.

Laboratory measurements have been made of the variation of B_z along the strap for the DIII-D antennas and both of the TFTR antennas. The results are shown in Table 6.2. The correction for the DIII-D antennas is much larger than that for TFTR (or for BPX, to be discussed later) because of a basic difference in design. In DIII-D, the single-end-fed current strap is grounded to a cavity sidewall near the front of the cavity rather than at the cavity backplane, as is the case for TFTR and BPX.

Figure 6.21 shows edge density profiles measured on DIII-D in both L-mode and H-mode operation for two different antenna designs.[22] The tokamak and antenna dimensions and the quantities required for the RANT model are shown in Table 6.3. Measured values of loading resistance for these plasma parameters are shown in Fig. 6.22 as the distance between the separatrix and the front

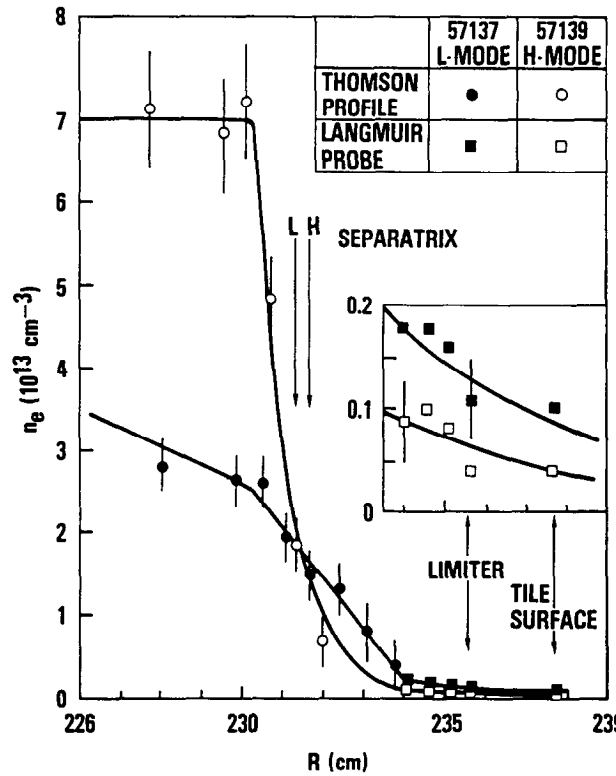

Fig. 6.21. Density profiles measured on DIII-D with the Thomson scattering system and the movable Langmuir prove during NBI L-mode and ELM-free H mode conditions. The insert shows Langmuir probe data with a magnified vertical scale. The radial locations of the separatrix. The outboard limiter and vessel tile surfaces are also indicated. The solid curves are the analytic fits to the data used in the Brambilla coupling code (from Ref. 18).

of the antenna protection tiles is varied.[22] The curves shown are theoretical loading predictions obtained with a modified version of the Brambilla antenna modeling code.[23] To model the H-mode results, we assumed a piecewise linear density profile that is flat from the magnetic axis out to a break radius $R_B = R_0 + r_B$, decays linearly to the separatrix radius, and has an exponential decay with characteristic length λ_S out to the antenna location:

$$n_e(r) = \begin{cases} n_0, & 0 \le r \le r_B \\ n_{sep} + (n_0 - n_{sep}) \left(\frac{r_{sep} - r}{r_{sep} - r_B} \right), & r_B \le r \le r_{sep} \\ n_{sep} e^{-(r - r_{sep})/\lambda_s}, & r_{sep} \le r \le r_{tile} \end{cases}$$

where the relevant plasma parameters are $n_0 = 7 \times 10^{13}$ cm^{-3}, $n_{sep} = 1.0 \times 10^{19}$ m^{-3}, $R_B = 2.3$

Table 6.2. Measured Values of $(h_s)_{eff}$

		Actual Length	Effective Length
TFTR	Bay-L	0.68 m	0.592 m
	Bay-M	0.76 m	0.602 m
DIII-D	Single Strap	0.45 m	0.275 m
	FWCD	0.45 m	0.275 m

Table 6.3. DIII-D Parameters

Tokamak Dimensions

R_{maj}	R_{axis}	R_{sep}	r_{sep}	R_{lim}		r_{lim} R_{tile}	r_{tile}
167	167	$230 \rightarrow 234$	$63 \rightarrow 67$	236	69	238	71

Parameters of Recessed Antenna Model

	a	b	d	d_s	W_s	W_c	h_s
Antenna I	10.1	5.1	$r_{front} - r_{tile}$	$r_{tile} - r_{sep}$	15.2	32.4	35.1
Antenna II	14.7	3.1	$r_{front} - r_{tile}$	$r_{tile} - r_{sep}$	15.2	32.4	35.1

Table 6.4. TFTR Antenna Parameters

Antenna	W_s	W_c	W_A	a	b	d	d_s
Bay L, strap 3	11	23	24.4	16.2	4.7	0.1	$r_{edge} - r_{sep}$
Bay L, strap 4	11	23	24.4	16.2	4.7	0.1	$r_{edge} - r_{sep}$
Bay M, slots	10	29	33.7				$r_{edge} - r_{sep}$
Bay M, no slots	10	29	33.7	15.7	3.2	0.1	$r_{edge} - r_{sep}$

Antenna	r_{sep}	r_{edge}	r_{wall}	r_{strap}	r_{cav}
Bay L, strap 3	96	101	101	105.8	122
Bay L, strap 4	96	100	100	104.8	121
Bay M, slots	96	100	106.7	103.3	119
Bay M, no slots	96	100	100.1	103.3	119

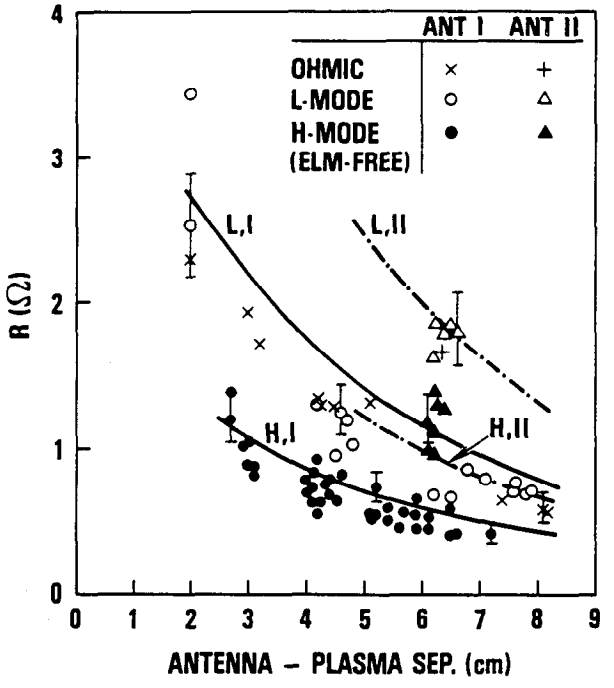

Fig. 6.22. Comparison of the antenna loading resistance for DIII-D antenna I and antenna II geometries as a function of δ_{ant}. Solid curves: Brambilla code with antenna I geometry. Dash-dot curves: Brambilla code with antenna II geometry (from Ref. 18).

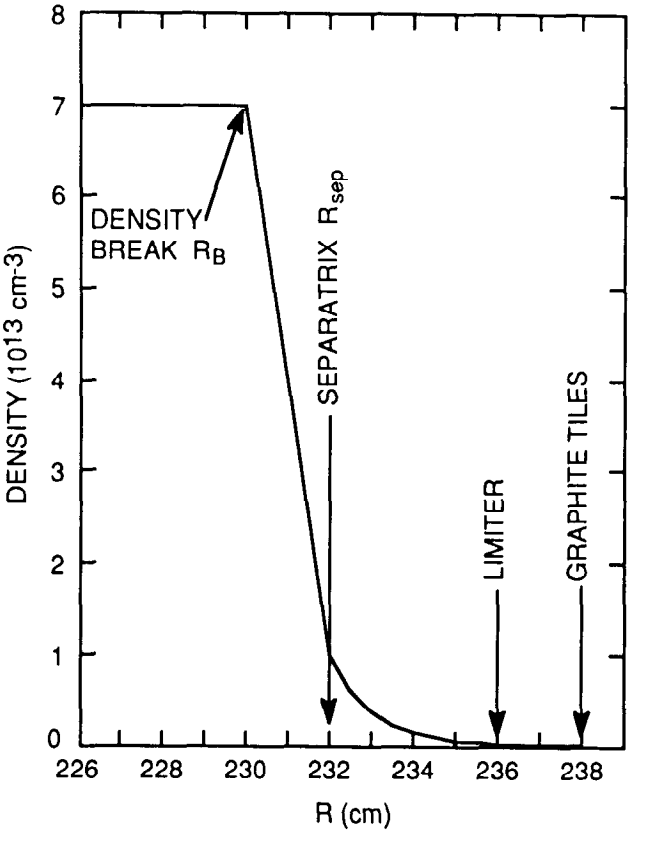

Fig. 6.23. Density profile used in RANT modeling of DIII-D antenna loading results for measured profile shown in Fig. 6.21.

m, $R_{sep} = 2.32$ m, $\lambda_S = 0.01$ m, $B_0 = 2.1$ T, and $f_{RF} = 31.8$ MHz.

This profile is plotted in Fig. 6.23 and is seen to overlay accurately with the experimental profile shown in Fig. 6.21. The RANT predictions are shown in Fig. 6.24 for the H-mode profiles for both antennas. To obtain these results, R' was calculated, then multiplied by the effective length presented in Table 6.2. These curves overlay very well with the experimental values and also agree closely with the Brambilla code results.

Calculations were also carried out for the TFTR Bay-M and Bay-L antennas. The geometric parameters of these antennas are shown in Table 6.4. There are differences in design (primarily narrower strap separation and greater strap-plasma distance for Bay-L) that make the loading characteristics of these antennas quite different. Unfortunately, there are no detailed edge density profiles available. However, there is some information about density somewhat inside the limiter radius, $R = 0.86$ m, for some shots where loading measurements were made. We have considered loading measurements on TFTR done with a 2.615-m major radius and 0.965-m minor radius (the plasma size is fixed by the inner limiter at 1.65 m). We have considered a case in which $\langle n_{el} \rangle = 5 \times 10^{21}$ m^{-2} and $n_e(r = 0.86$ m$) = 1.1 \times 10^{19}$ m^{-3} (as determined by the last radial channel of the interferometer). By extrapolating the interferometer and Thomson scattering profile data, we estimate the density at the separatrix to be $n_{sep} = 3.7 \times 10^{18}$ m^{-3}. In this case, R_{sep} refers to the limiter radius. To model this, we have used a power-parabolic density profile of the form

$$n_e(r) = \begin{cases} (n_0 - n_{sep})[1 - (r/R_{sep})^2]^{\alpha_N} + n_{sep} & \text{for } 0 \le r \le R_{sep} \\ n_{sep} e^{-(r-R_{sep})/\lambda_s} & \text{for } R_{sep} \le r \le R_{edge} \\ 0 & \text{for } R_{edge} \le r. \end{cases}$$

Choosing $n_0 = 3.63 \times 10^{19}$ m^{-3} and $\alpha_n = 0.887$, this profile satisfies the density constraints above.

Table 6.5. Antenna Loading Result for TFTR

Antenna	R' (Ω/m)	$(h_s)_{eff}$(cm)	R (Ω)	Experimental R (Ω)
Bay-M	13 → 15	62.4	8 → 9	9 → 10 (J. Hosea[3])
Bay-L	3.4 → 5	59.7	2 → 3	2 → 2.5 (D. J. Hoffman[24])

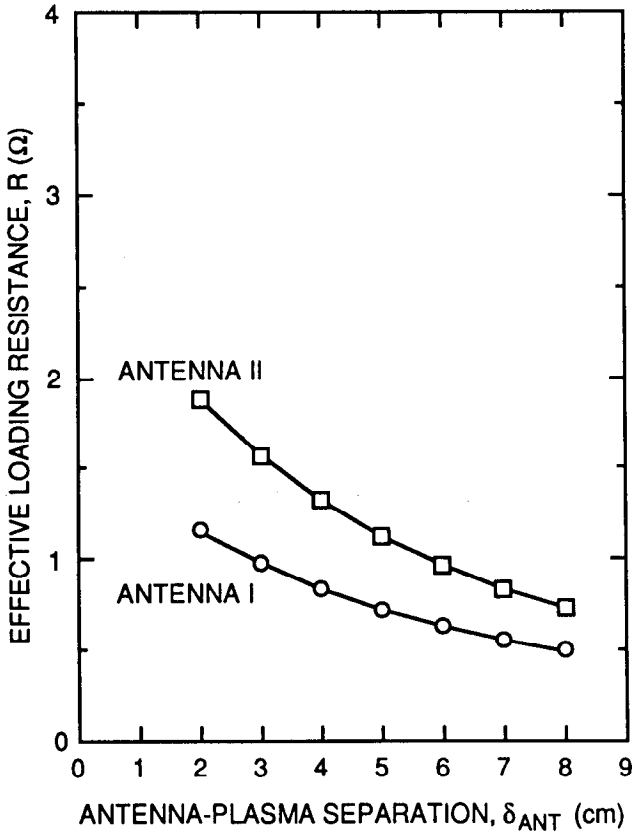

Fig. 6.24. RANT results for same loading measurements as shown in Fig. 6.22.

The decay length in the scrape-off region was chosen to be $\lambda_s = 0.01$ m, although n_{sep} is so small that the results are completely insensitive to λ_s. The results are shown in Table 6.5.

The range of calculated values for R' represents an attempt to model the effect of slotted sidewalls in the antenna enclosure. This was done by varying the location of the vessel wall in the model from several centimeters in front of the current strap to just at the current strap. One can see that the model closely matches the observed values and correctly predicts the large difference in loading between the Bay-L and Bay-M antennas.

VI.C.4. Loading Calculations for BPX

With the agreement between theory and experiment and among the different antenna codes illustrated in the previous section, we have considerable confidence in our ability to predict loading for BPX antennas, if the edge density profile were known. Loading calculations have been done for a number of different antenna designs and different density profiles. Scans over various design parameters such as strap width, strap separation, and recess depth have been done to quantify trends and trade-offs. Here we will concentrate on the results that have set the design parameters; that is, we consider the BPX hybrid antenna design and concentrate on very flat profiles which represent the worst case for loading.

Table 6.6 shows the dimensions used in the modeling.

We have already stated that the loading is a sensitive function of edge density profile. Figure 6.25 shows the change in profile shape as the parameter α_N varies from 0.5 (square-root parabolic) to 0.0 (flat). For this plot, the scrape-off decay length was $\lambda_s = 1$ cm and $n_{sep} = 0.1\ n_0$. Figure 6.26 shows loading of a slightly earlier version of the hybrid antenna for this set of profiles for various values of λ_s. For these calculations, n_0 was adjusted to maintain the volume-average density constant at $\langle n_e \rangle = 2 \times 10^{20}$ m^{-3}. At this density, loading is a decreasing function of profile steepness, $\alpha_n \to 0$ and an increasing function of scrape-off length. Also shown is the flat profile point, $\alpha_n = 0$, $\lambda_s = 0$, for which the plasma surface impedance was obtained from the plasma dispersion relation rather than by integrating the differential equation. We see that the diffuse profile results converge properly to the flat profile results, even in the limit of very steep profiles.

It is known that H-mode density profiles can be flat with very steep gradients just inside the separatrix (see Fig. 6.21) To model this, we again use a

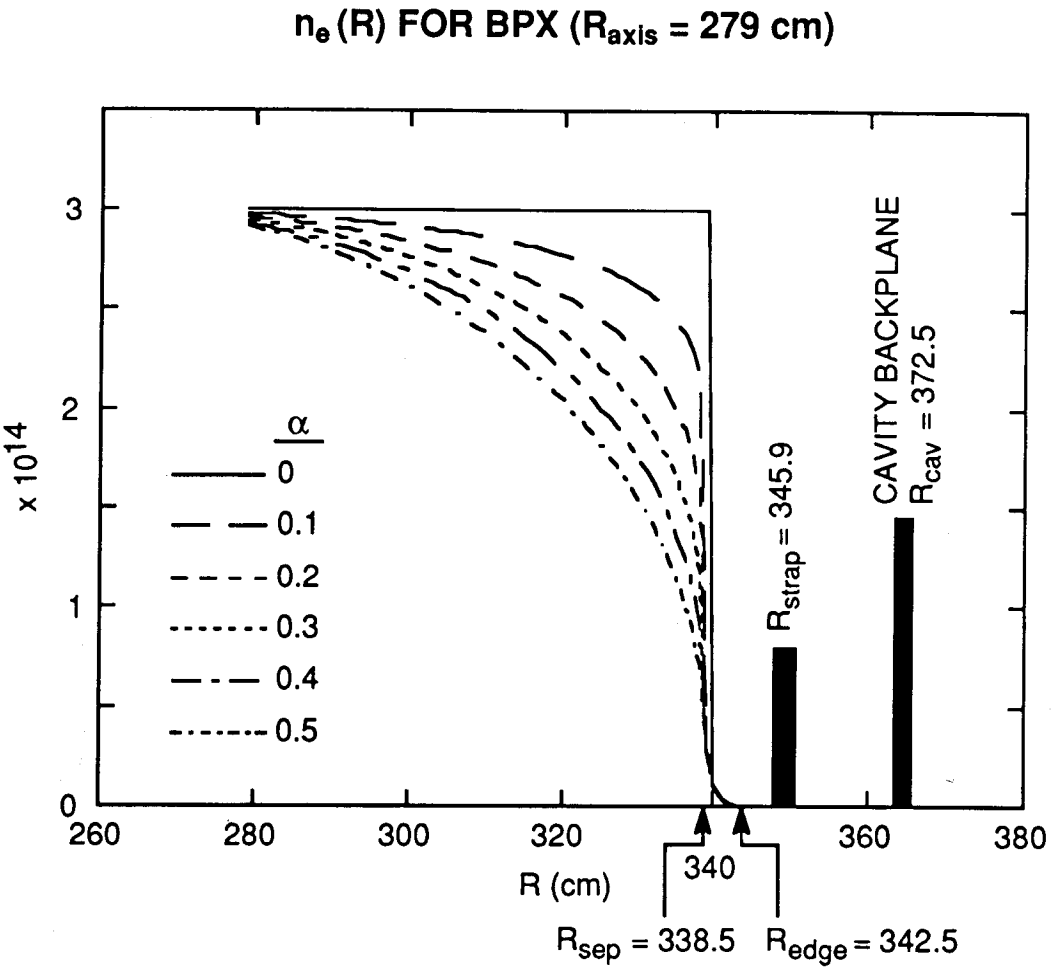

Fig. 6.25. Power-parabolic density profiles $\{\sim [1-(r/r_{sep})^2]^{\alpha}\}$ converging to flat ($\alpha \to 0$) profile.

Table 6.6. BPX Antenna Parameters

Tokamak Dimensions

Antenna	R_{maj}	R_{axis}	r_{cav}	r_{strap}	r_{wall}	r_{sep}	r_{edge}
Hybrid	259	259	113.5	86.9	86.8	76 → 81	83.5

Parameters of Recessed Antenna Model

Antenna	a	b	d	d_s	W_s	W_c	W_A	h_s
Hybrid	26.6	0.1	3.3	3 → 8	14.6	29.3	30.5	47.9

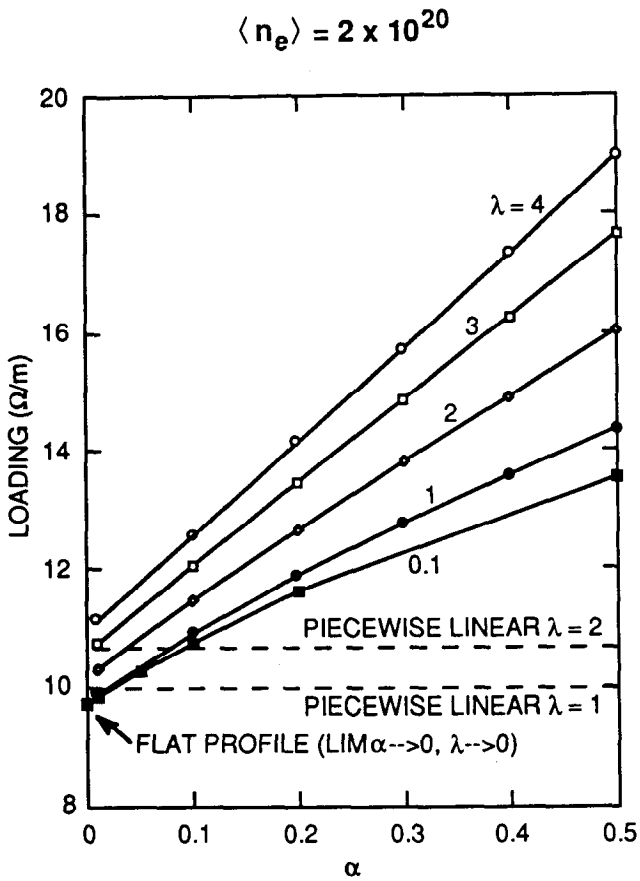

Fig. 6.26. Antenna loading, R', versus profile shape exponent, α.

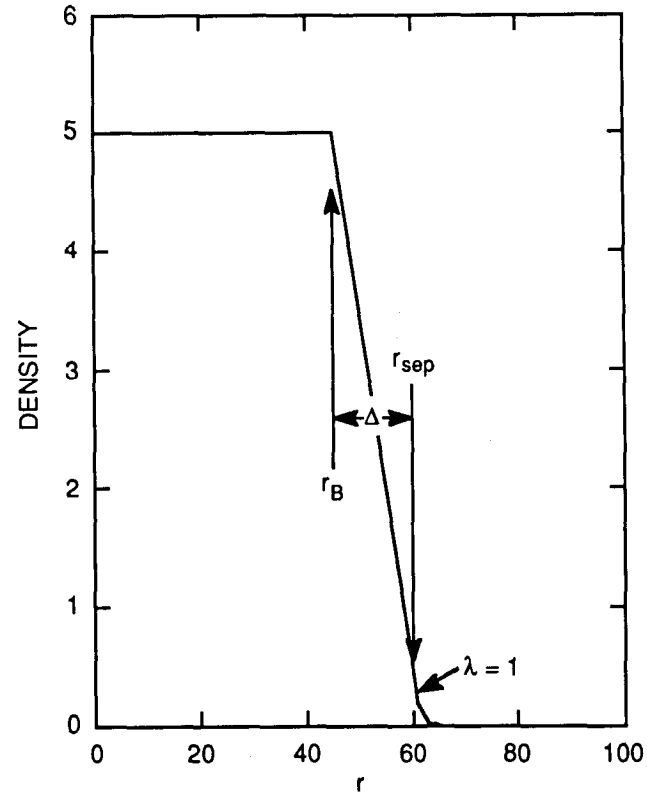

Fig. 6.27. Geometric parameters for piecewise linear density profile used to model H-mode loading in Figs. 6.28, 6.29, and 6.30.

piecewise linear model, Fig. 6.27. We assume the location of the front of the antenna to be fixed relative to the magnetic axis r_{edge}. We vary d_s, the separation between the front of the antenna and the separatrix, by adjusting $r_{sep} = r_{edge} - d_s$. And we adjust the steepness of the profile by adjusting $\Delta = r_{sep} - r_b$. The nominal antenna-separatrix spacing is $d_s = 0.04$ m. A poloidal limiter extends radially to 0.01 m inside the Faraday shield. A belt limiter extends in an additional 0.01 m. The nominal separatrix position is 0.02 m inside the belt limiter.

Figures 6.28, 6.29, and 6.30 show loading for the hybrid antenna for a low-density case ($\langle n_e \rangle = 1 \times 10^{20}$ m^{-3}), a nominal-density case ($\langle n_e \rangle = 2.5 \times 10^{20}$ m^{-3}), and a high-density case ($\langle n_e \rangle = 5 \times 10^{20}$ m^{-3}), respectively. In all cases, the density at the separatrix is taken to be 10% of the peak density. The current straps are driven out of phase (dipole phasing). These results can be qualitatively understood by considering the two competing physical effects involved:

1. Increasing the plasma density near the antenna (increased λ_s or decreased d_s) reduces the evanescence distance through which the waves must tunnel in order to propagate, thus increasing loading.
2. A steep density gradient in front of the antenna [increased $n_e(R_B)$ or decreased Δ] presents an impedance mismatch which decreases coupling.

At low density (Fig. 6.28), the impedance mismatch is minimal so the main effect of increasing Δ (decreasing steepness) is to reduce the amount of nearby plasma and decrease coupling. At higher densities, the impedance mismatch is important so that increased Δ increases loading. However, moving the density discontinuity closer to the current strap (smaller d_s) decreases the tunneling distance and therefore increases loading at both high and low $\langle n_e \rangle$.

It is of interest to compare these results with calculations obtained from the ORION two-

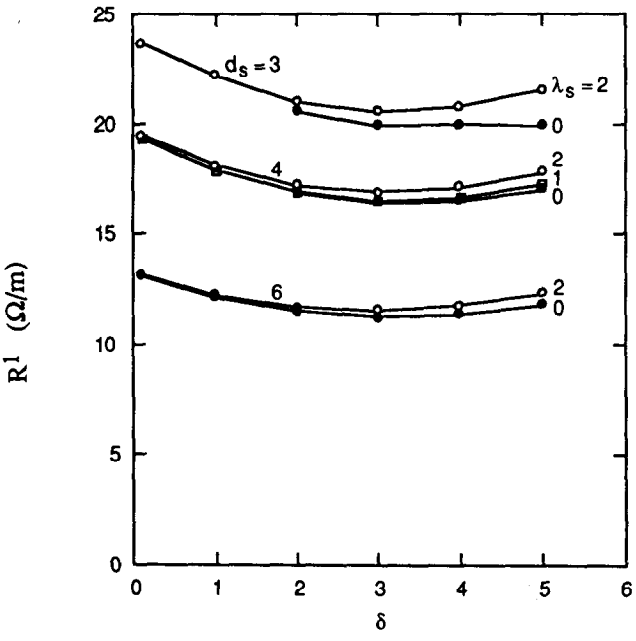

Fig. 6.28. Loading for BPX hybrid antenna versus Δ for various Faraday shield-to-separatrix separations d_s and scrape-off decay lengths λ_s: low-density case ($\langle n_e \rangle = 1.0 \times 10^{20}$ m^{-3}).

dimensional code. The geometric parameters for the ORION calculations presented in Figs. 6.14, 6.13, and 6.16, correspond to $d_s = 4$ cm, $\lambda_s = 2$ cm, and $\Delta = 5$ cm, shown for the RANT model in Fig. 6.29. The ORION value for loading resistance is $R' = 19.34$ Ω/m, obtained by dividing the total absorbed power by the 96-cm strap height and by 2 for the number of current straps. This is to be compared to the RANT value of 21 Ω/m. There are some differences in the two models that should be borne in mind in this comparison. The ORION code includes reflection at the fast-wave cutoff for low-$k_\parallel$ modes, which reduces loading relative to RANT (which has purely outgoing wave boundary conditions). Image currents included in ORION in the walls at the top and bottom of the straps introduce some end effects, although the geometry at the end of the current straps is not an accurate representation of the actual design. This would also reduce loading relative to RANT. The finite poloidal length of the current straps is correctly included in ORION (higher poloidal modes are slightly more evanescent than the uniform poloidal fields of RANT). The finite phase velocity effect is not included since the current was assumed uniform in the poloidal direction. Image currents in the side walls, which are correctly included in RANT, are absent in the ORION calculations. This would tend to increase the ORION loading relative to RANT. Altogether the agreement between codes seems quite good despite the differences in the models.

It is clear that the critical issue is loading at the highest volume-average density, with steep profiles ($\Delta \sim 0$) and with very little plasma in the scrape-off layer. Therefore, the reference profile for specification of the RF system is the worst case of a flat density profile, $\Delta = 0$, with no scrape-off plasma, $\lambda_s = 0$. We see from Fig. 6.30 that at the nominal separatrix location, $d_s = 4$ cm, the minimum loading is 8.6 Ω/m. This is the basis for adopting a value of $R' = 8.6$ Ω/m as the reference design value of load resistance. This value is further reduced by an end-effect factor of 0.92 as obtained by scaling from measurements on the TFTR antenna.

Note that the flat reference profile is in fact nonphysical. If the density gradient just inside the separatrix is not permitted to be infinite and if some plasma is assumed to be in the scrape-off layer, then predicted loadings are higher. For example, if the fall-off distance Δ is 2 cm and the scrape-off distance λ_s is 1 cm, then for the nominal limiter position, $d_s = 4$ cm, the loading is $\simeq$12 Ω/m, a factor of 1.4 larger than the reference value.

As a further point of reference, the recessed antenna code ANTIMP, developed at the University of Wisconsin, has been used[21] to consider a piecewise linear density profile with a flat region in the center. This profile has the following parameters: $n_e(0) = 4 \times 10^{20}$ m^{-3}, $n_e(r_B) = 3 \times 10^{20}$ m^{-3}, $f_{RF} = 85$ MHz, $\Delta = 1$ cm, $d_s = 4$ cm, and $\lambda_s = 1$ cm. Note that this density profile is a good fit to a parabolic profile with power exponent $\alpha = 0.25$. As in RANT, the antenna is enclosed in a box of finite length in the toroidal direction, and ANTIMP explicitly takes into account finite k_y effects. With a uniform current in the poloidal direction, ANTIMP gives a loading resistance R_L of 9.5 Ω for dipole phasing. Applying an end-effect correction factor of 0.92, we obtain $(R_L)_{RANT} = 8.75$ Ω for this case. Letting the parameter Δ vary from 1 to 10 cm, the loading resistance changes from 9.5 to 17.6 Ω, respectively. A modified version of the Brambilla code[20] has also been used to study the variation of R_L with respect to the wave phase velocity v_p along the strap. For a four-coaxial feed case (in which the current distribution does not greatly deviate from uniformity) and plasma parameters corresponding to BPX L and H modes, R_L decreases by 18% as the phase velocity along the coil decreases from that producing a uniform current to 0.6 times the speed of light in vacuum.

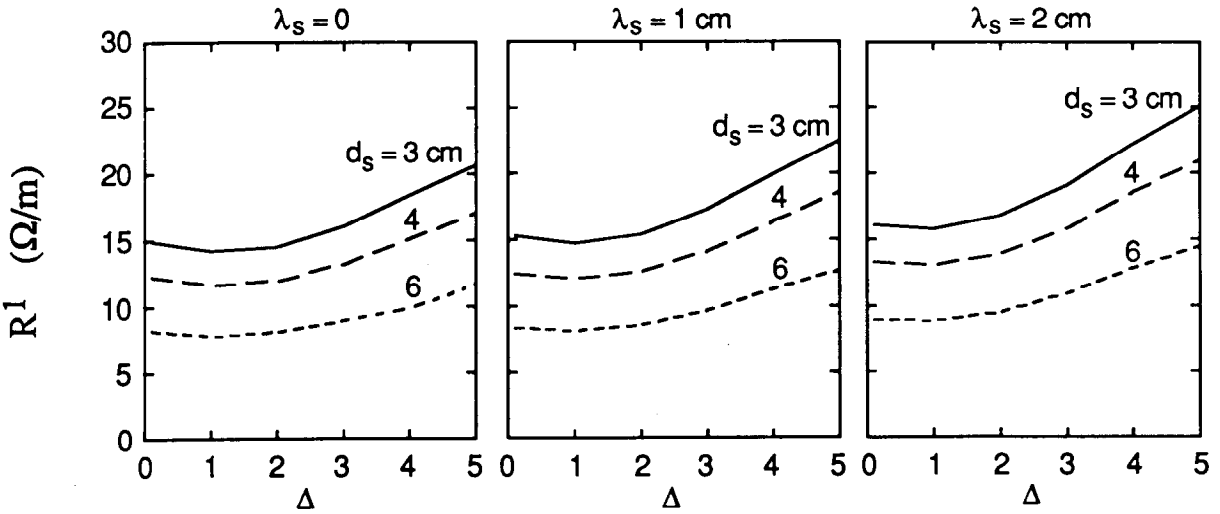

Fig. 6.29. Loading for BPX hybrid antenna versus Δ for various Faraday shield-to-separatrix separations d_s and scrape-off decay lengths λ_s: intermediate-density case ($\langle n_e \rangle = 1.0 \times 10^{20}$ m^{-3}).

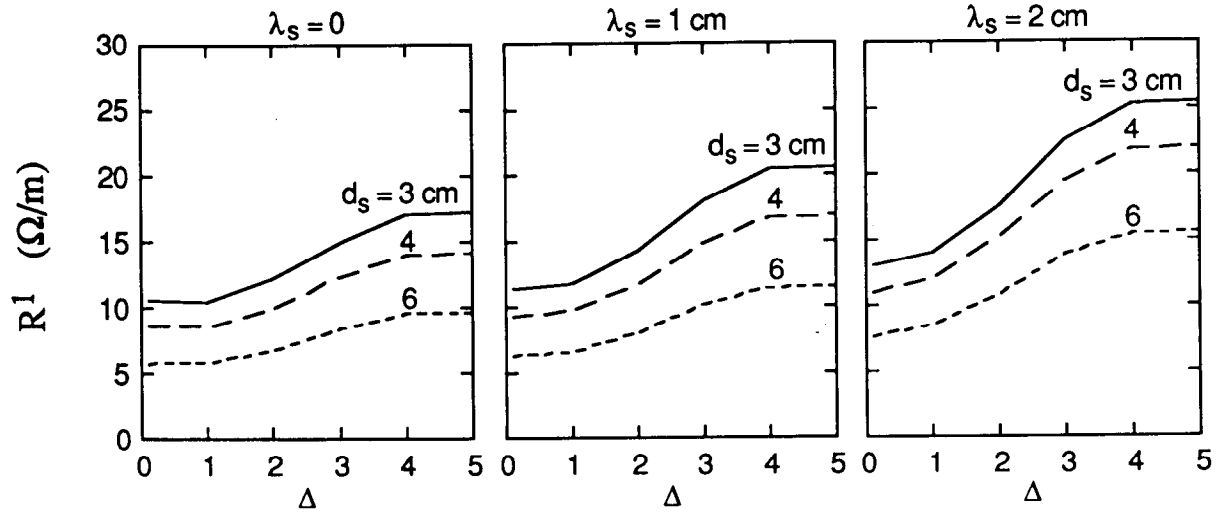

Fig. 6.30. Loading for BPX hybrid antenna versus Δ for various Faraday shield-to-separatrix separations d_s and scrape-off decay lengths λ_s: high-density case ($\langle n_e \rangle = 1.0 \times 10^{20}$ m^{-3}).

VI.C.5. Faraday Shield Design Issues

The Faraday shield is the final interface between the RF hardware and the plasma that is to be heated. Details of the plasma particle and energy fluxes in the scrape-off region along with RF losses control the heat load on the shield. These fluxes, together with the structure of RF near fields and RF-driven sheaths, determine the degree of local sputtering, impurity generation, and outgassing. Forces generated by induced currents during disruption place severe constraints on Faraday shield design for survivability. In turn, the Faraday shield affects the plasma through its proclivity to generate impurities, through its behavior as a limiter, and by its effect on the RF fields that ultimately must penetrate to the plasma.

There is a substantial base of empirical information on Faraday shield behavior in high-power tokamak experiments. Many designs have been tried, and data exist on the influence of blade size and shape, blade angle with respect to the magnetic field, and structural and coating materials (see Ref. 25 for many relevant papers and additional references). There is also beginning to be a base of physics understanding on Faraday shield effects in ICRF plasmas and in particular on how impurities are generated. Several mechanisms have been identified and investigated for the generation of enhanced sheath potentials due to RF fields.[26–28]

A model has been developed that has been quite successful in explaining observations of impurity influx on JET in terms of sputtering due to ion acceleration in the rectified direct current (DC) sheath potential.[29] This model, combined with experience with various antenna designs, gives guidance as to the important variables for minimization of impurity influx. To the extent that impurity generation is a result of enhanced sheaths, the critical element is to minimize the peak voltage of the RF-rectified sheaths. The sheath potential is limited by line integral of the RF electric field along a magnetic field line that couples two grounded metal surfaces, such as two Faraday shield blades, of the front face of a Faraday shield blade and a limiter. This line integral is equal to the RF magnetic flux linked by the magnetic field line, which is in turn proportional to the antenna strap current or strap voltage. It is therefore important to minimize the possible flux linkages by aligning the Faraday shield blades as nearly parallel to the tokamak magnetic field as possible and by contouring the shield to the flux surfaces to minimize linkages to nearby limiters. Operation with two symmetric current straps, driven out of phase, also greatly reduces the RF flux linked by magnetic field lines at the front face of the shield. Since at fixed radiated power the RF voltage is inversely proportional to the loading resistance, it is clear that high loading resistance is important for impurity control as well as for control of breakdown at the high-voltage points in the transmission system. Another important parameter is the plasma density at, and just in front of, the Faraday shield. This is because both the potential of the rectified sheath and the flux of sheath accelerated ions onto the surface increases with density.

Finally, it is clear that the materials used in the surfaces of Faraday shield elements and limiters is of critical importance. High-Z materials such as nickel, molybdenum, and tungsten are subject to high self-sputtering yields when sheath potentials exceed a few hundred volts. Fortunately, there exist low-Z materials with the requisite thermal and mechanical properties to be usable in this environment and that have sputtering yields for normal incidence less that 1 at all energies. Beryllium and graphite are in this category. Calculations by D'Ippolito et al.,[30] in a model that includes ion acceleration in RF-enhanced sheaths, physical sputtering, and scrape-off layer physics, have shown that amplification of neutral metal production by self-sputtering can lead to an avalanche phenomenon in high-Z surface materials, which is absent or significantly weaker with low-Z surface materials such as beryllium or carbon.

Another parameter that may be relevant because of its influence on the RF ponderomotive force on the plasma in front of the antenna is the RF power density in watts per square meter. The power density for the BPX hybrid antenna at $\sim$8.5 W/m^2 is substantially above that at which JET typically operates. However, it is comparable to the power densities achieved on TFTR and is well below the operating level of 12 MW/m^2 achieved on JT-60.

The BPX hybrid antenna system has been designed according to the above principles. Although design work for the BPX hybrid antenna Faraday shield is ongoing, an idea of the present concept can be obtained from Figs. 6.17a, 6.17b, and 6.17c. A single tier of shield tubes is planned, the tubes being angled to align as closely as possible with the magnetic field. The shield is to be constructed of copper-plated Inconel tubes with carbon-carbon composite tiles mechanically attached to the plasma side of the tubing (see inset, Fig. 6.17a). A single-tier design allows the current strap to be brought closer to the plasma than with a double-tier design, substantially increasing the antenna coupling. Furthermore, a more open design with wider spacing between tubes results in an increase in magnetic flux transmission of approximately 10%. The carbon-carbon composite has much higher electrical conductivity than con-

ventional graphite and allows smaller RF heating of the shield but has better thermal properties for disruption shocks than beryllium.

It must be made clear that the engineering difficulties of designing a Faraday shield for BPX are severe. Heat loads from the plasma are large, and for certain materials, such as graphite, ohmic dissipation of the RF fields provides additional large heat loads. The shield must withstand large disruption forces. Therefore, information from the new antennas on JET and those being constructed for TFTR, Alcator C-Mod, and JT-60U will be monitored closely. Information coming from these experiments will be factored into the BPX design as it becomes available. A backup design will be considered along the lines of the JET wall-mounted antenna concept. This may permit more power to be launched per port or allow the power density in watts per cubic meter to be decreased at constant power. In addition, an array of uniformly spaced current straps could provide more control of the $k_{\|}$ spectrum for such purposes as current drive.

VI.C.6. Summary

ICRF appears to be ideally suited to heating the high-density plasmas of BPX. Present-day experiments have achieved the ICRF power levels required for BPX and have achieved plasma parameters approaching the BPX regime. The baseline heating scenario for BPX, ^{3}He minority in D-T plasma, is similar to the D(^{3}He) scenario that is routinely used in present experiments. A sizable base of experience now exists on a number of tokamaks, which permits confidence in extrapolation to the use of ICRF on BPX. Theoretical calculations, which have been found to be broadly consistent with experimental results, predict excellent heating for BPX plasmas. Although there is a significant amount of research, theory/experiment comparison, and model development to be done in order to ensure optimum ICRF performance and to develop possibilities for alternative scenarios, there is no reason to doubt the success of ICRF in BPX.

Design of an ICRF system for BPX, particularly the launching structures, is a technological challenge. Heat loads and disruption stresses are severe, and remote maintenance problems are difficult. These factors have been analyzed and an antenna design obtained that meets the system design requirements (see the System Design Description for details). The launching efficiency of this design has been analyzed in detail, and consideration has been given to a wide range of plasma density profiles that might be confronted. The design is conservative from a power radiation point of view, in that the required power can be coupled into the most unfavorable density profile with moderate peak voltages in the RF system (32.5 kV). Careful attention has been paid to experience gained in JET, TFTR, JT-60, PLT, and other high-power experiments to minimize breakdown and impurity generation problems. This is an ongoing process, and new information on antenna and Faraday shield performance as well as materials properties will be incorporated as it becomes available. It is also planned to do further investigation of design concepts other than the hybrid, for example, a wall-mounted concept, in the spirit of the JET configuration.

ACKNOWLEDGMENTS

Research sponsored by the Office of Fusion Energy, U.S. Department of Energy, under contract DE-AC05-84OR21400 with Martin Marietta Energy Systems, Inc.

REFERENCES

1. D. START, JET, Private Communication.

2. D. START et al., *Proc. 13th Int. Conf. on Plasma Physics and Controlled Nuclear Fusion Research,* Washington, D.C., October 1–6, 1990, International Atomic Energy Agency (1990).

3. J. HOSEA et al., *Proc. 13th Int. Conf. on Plasma Physics and Controlled Nuclear Fusion Research,* Washington, D.C., October 1–6, 1990, International Atomic Energy Agency (1990).

4. JET Team, *Proc. 11th Int. Conf. on Plasma Physics and Controlled Nuclear Fusion Research,* Kyoto, Japan, November 13–20, 1986, IAEA-CN-47/F-I-1, p. 449, International Atomic Energy Agency (1986).

5. D. F. H. START et al., *Proc. 12th Int. Conf. on Plasma Physics and Controlled Nuclear Fusion Research,* Nice, France, October 12–19, 1988, IAEA-CN-50/E-II-3, p. 593, International Atomic Energy Agency (1988).

6. J. HOSEA et al., *Proc. 8th Int. Conf. on Plasma Physics and Controlled Nuclear Fusion Research,* Brussels, Belgium, July 1–10, 1980, IAEA-CN-38/D-5-1, Vol. II, p. 95, International Atomic Energy Agency (1980).

7. T. K. MAU and D. A. EHST, *Bull. Am. Phys. Soc.,* **34,** 1968 (1989).

8. E. F. JAEGER et al., *Nucl. Fusion,* **28,** 1 (1988) and references contained therein.

9. J. R. WILSON et al., *Proc. 12th Int. Conf. on Plasma Physics and Controlled Nuclear Fusion Research,* Nice, France, October 12–19, 1988, International Atomic Energy Agency (1988).

10. D. SMITHE et al., *Phys. Rev. Lett.,* **60,** 801 (1988).

11. E. F. JAEGER et al., *Nucl. Fusion,* **30,** 505 (1990).

12. R. WHITE et al., *Phys. Fluids B,* **2,** 745 (1990).

13. B. COPPI et al., *Phys. Fluids B,* **2,** 927 (1990).

14. J. ONGENA et al., *Proc. of 17th European Conf. on Controlled Fusion and Plasma Heating,* Amsterdam, Netherlands, June 25–29, 1990, Vol. 14B, Part 1, p. 383, European Physical Society (1990).

15. F. PORCELLI et al., *Proc. of 17th European Conf. on Controlled Fusion and Plasma Heating,* Amsterdam, Netherlands, June 25–29, 1990, Vol. 14B, Part 1, p. 327, European Physical Society (1990).

16. J. HOSEA et al., *Proc. of Joint Varenna-Lausanne Int. Workshop on Theory of Fusion Plasmas,* Varenna, Italy, August 27–31, 1990.

17. D. J. CAMPBELL et al., *Phys. Rev. Lett.,* **60,** 2148 (1990).

18. R. GOULDING, ORNL, Private Communication.

19. J. S. TOLLIVER and D. B. BATCHELOR, *Bull. Am. Phys. Soc.,* **34,** 2035 (1989).

20. M. BRAMBILLA, *Nucl. Fusion,* **28,** 549 (1988).

21. J. E. SCHARER, N. T. LAM, M. BETTENHAUSEN, and J. RUFINUS, UW-CPTC Report 90-7, University of Wisconsin (1990).

22. M. MAYBERRY et al., *Nucl. Fusion* **30,** 579 (1990).

23. S. C. CHIU, M. J. MAYBERRY and W. D. BARD, *Nucl. Fusion,* **30,** 2551 (1990).

24. D. J. Hoffman, ORNL, Private Communication, 1991.

25. J. M. NOTREDAEME and D. B. BATCHELOR, *Fusion Eng. Design,* **12** (1990).

26. F. W. PERKINS, *Nucl. Fusion,* **29,** 583, (1989).

27. R. CHODURA, *Fusion Eng. Design,* **12,** 111 (1990).

28. M. D. CARTER et al., *Fusion Eng. Design,* **12,** 105 (1990)

29. J. R. MYRA, D. A. D'IPPOLITO, and M. J. GERVER, *Nucl. Fusion,* **30,** 845, (1990).

30. D. A. D'IPPOLITO et al., "A Model of Sheath-Driven Impurity Production by ICRF Antennas," LRC-90-18, Lodestar Research Corp. (1990).